Calibration and Cross Validation of a Global Wind and Wave Database of Altimeter, Radiometer, and Scatterometer Measurements

I. R. YOUNG, E. SANINA, AND A. V. BABANIN

Department of Infrastructure Engineering, University of Melbourne, Parkville, Victoria, Australia

(Manuscript received 24 July 2016, in final form 24 March 2017)

ABSTRACT

A combined satellite dataset consisting of nine altimeter, 12 radiometer, and two scatterometer missions of wind speed and wave height is calibrated in a consistent manner against NDBC data and independently validated against a separate buoy dataset. The data are investigated for stability as a function of time. Instances where there are discontinuities or drift in the data are identified and accounted for in the calibration. The performance of each of the instruments at extreme values is investigated using quantile–quantile comparisons with buoy data. The various instruments are cross validated at matchup locations where satellite ground tracks cross. The resulting calibrated and cross-validated dataset is believed to represent the largest global oceanographic dataset of its type, which includes multiple instrument types calibrated in a similar fashion.

1. Introduction

Oceanographic satellites have now been in operation for more than 30 years, providing an almost continuous record of wind speed and wave height with global coverage. Such data have become routinely used in a range of applications such as offshore engineering design, testing of numerical models, studies of air–sea fluxes, wind and wave climatology, and the investigation of trends in oceanographic wind speed and wave height. Four main instruments that provide global measurements of wind speed and/or wave height have been operational during this period—altimeters, radiometers, scatterometers, and synthetic aperture radars. These systems have been carried on more than 20 different satellite missions.

Each of these missions is a valuable data source. However, the full value of such data is achieved through the long-term nature of the combined record. To realize this value, the full dataset needs to be consistently calibrated, validated, and cross validated. Once this has been achieved and there is consistency across the instruments, the added value of a long-term combined database can be realized.

This paper describes the calibration of all these platforms against an extensive buoy dataset and its validation against an independent buoy dataset (see the appendix tables). The instruments are checked for long-term stability and where discontinuities or drift is observed, such issues are corrected. Where multiple satellites are in orbit at the same time, the instruments on board are cross validated. In addition to ''scatterplot'' calibrations, which are weighted to mean conditions, the structure of the probability distribution function is examined for each instrument. This enables an assessment to be made of the performance of instruments in measuring extreme conditions. An error analysis considers the potential errors in calibration against buoy data and attempts to reconcile differences with previous calibrations of individual instrument types. The resulting dataset is believed to be unique, bringing together data from 23 missions using three different instrument types (synthetic aperture radar is not used).

The structure of the paper is as follows. Section 2 provides an overview of satellite remote sensing of the oceans. Section 3 provides a description of the satellite platforms and the instruments they carried, which make up the present database. This is followed by a description of the calibration of the satellite data against in situ buoy data, an assessment of the long-term stability of the datasets, and an examination of the probability distribution functions (section 4). Section 5 reports on the cross validation between satellite platforms that were operational at the same time. An error

Corresponding author: Ian Young, ian.young@unimelb.edu.au

DOI: 10.1175/JTECH-D-16-0145.1

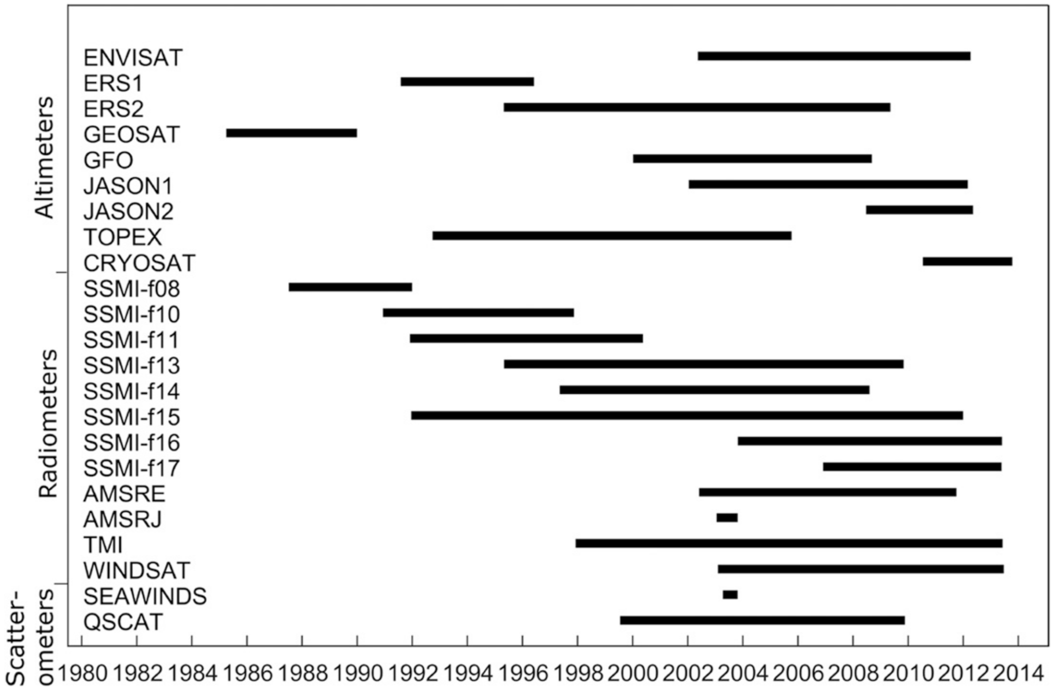

FIG. 1. Durations of satellite missions included in the combined database.

analysis is considered in section 6, including comparisons with previous studies. Finally, conclusions are reported in section 7.

2. Satellite remote sensing of the oceans

a. Radar altimeters

Since the launch of *Geosat* in 1985, there has been an almost continuous coverage of global altimeter data (see Fig. 1). The altimeter images a footprint between 5 and 10 km in diameter. Based on the shape and intensity of the returned radar signal from this footprint, the altimeter can estimate the significant wave height H_s and wind speed U_{10} (Cheney et al. 1987; Walker 1995; Chelton et al. 2001; Queffeulou 2004; Young 1994, 1999; Zieger et al. 2009). The significant wave height is estimated from the slope of the leading edge of the return pulse (Chelton et al. 2001; Holthuijsen 2007) and the wind speed from the energy of the return pulse, as measured by the radar cross section σ_0 (Chelton et al. 2001).

The satellites carrying altimeters have been placed in near-polar orbits. As a result, over a period of time, the satellite will image the full Earth. The along-track data density is of order 10 km; that is, an observation of H_s and U_{10} is made every 10 km along the ground track. After a period of time known as the Exact Repeat Mission (ERM), the satellite will fly over the same ground track. The ERM generally varies between 5 and 20 days depending on satellite orbit. As such, the separation between ground tracks at the equator can vary between 100 and 400 km. Therefore, although the along-track resolution of the altimeter is relatively high, its temporal and cross-track resolution is low (numbers of days/hundreds of kilometers). Hence, although such instruments provide global coverage, the low spatial/temporal resolution means that some storm events may be undersampled or missed completely (Young et al. 2011; Vinoth and Young 2011; Young et al. 2012; Zieger et al. 2014).

b. Microwave radiometers

A continuous record of radiometer measurements of the ocean commenced with the launch in 1987 of the Special Sensor Microwave Imager (SSM/I) *F8* instrument operating on polar-orbiting Defense Meteorological Satellite Program (DMSP) satellites. The radiometer measures the brightness temperature of the sea surface, which is related to the emissivity and reflection properties of the ocean. These in turn are a function of the roughness of the water surface and hence the wind stress. This wind stress is then related to the wind speed, usually assuming a neutrally stable atmospheric boundary layer and a constant value of the drag coefficient (Hollinger et al. 1990; Wentz 1997; Mears et al. 2001; Meissner and Wentz 2012).

The radiometer measures over a swath approximately 1400 km wide and produces measurements of wind speed (not direction) at a resolution of 25 km (Mears et al. 2001). These satellites are usually placed in sun-synchronous orbits, and the combination of ascending and descending passes images almost the full Earth each day. Hence, compared to altimeters, radiometers provide much greater spatial and temporal resolution. Generally, however, radiometers cannot provide reliable wind speed data in regions with heavy rain (Meissner and Wentz 2009).

c. Scatterometers

Like the altimeter, the scatterometer measures σ_0. By the use of either multiple fan antennas or a rotating disk pencil beam, scatterometers measure σ_0 from a range of different azimuth angles, thus also allowing the wind direction to be determined. The continuous coverage of global scatterometer data commenced in 1991 with the launch of *ERS-1*. As with the radiometer, scatterometer missions have generally utilized sun-synchronous near-polar orbits with a ground-track swath of up to 1400 km and a resolution of 25 km (Naderi et al. 1991; Kramer 1994; Henderson and Lewis 1998; Long and Drinkwater 1999; Spencer et al. 2000). Like radiometers, scatterometer measurements in the presence of heavy rain are generally not reliable.

d. Synthetic aperture radar

As its name suggests, the synthetic aperture radar (SAR) takes advantage of the "synthetic aperture" created by the forward motion of the satellite platform. This means that the resolution of the radar is far greater than one would expect given the physical size of the radar antenna. Synthetic aperture radars have flown on *ERS-1*, *ERS-2*, *Envisat*, RadarSat, TerraSAT, and Sentinel-1 missions, giving a near-continuous record since 1991. Although the forward motion of the satellite results in enhanced radar resolution, it also results in a number of complexities when imaging ocean waves. The relative motions of the satellite and surface waves means that the resulting transfer function relating the radar image to the directional surface wave spectrum is strongly nonlinear. The basic principles of operation were described by Alpers et al. (1981) and Hasselmann et al. (1985), and a process to obtain the full directional wave spectrum was first described by Hasselmann and Hasselmann (1991). Numerous refinements to such SAR inversion techniques have been developed, a summary being provided by Li et al. (2011).

Importantly, the SAR is the only instrument with the potential to measure the full directional wave spectrum and, as a minimum, the integral properties of the significant wave height, the mean/peak wave period, and the mean wave direction. Wave mode SAR images are typically 5 km × 10 km and spaced every 200 km along track (Li et al. 2011). As such, the spatial and temporal resolution is low. Although the potential for SAR is significant, the relatively low spatial/temporal resolution has limited its application. As such, SAR data have not been included in the present database. This situation will change in future years. The launch of instruments such as TerraSAR and more recently the Sentinel-1 mission means the long-term dataset of more spatially dense SAR imagery will rapidly grow.

e. Calibration/validation

It is common practice to calibrate satellite-based remote sensing systems against in situ buoys as well as against other satellite systems. However, there are few calibration and validation exercises that have attempted to ensure there are long-term consistent datasets by calibrating multiple instrument systems (e.g., combined altimeter and radiometer) in the same manner and then cross validating to ensure consistency. Some attempts have been made to produce consistent datasets from some altimeter missions (e.g., Cotton and Carter 1994; Callahan et al. 1994; Young 1998b; Alves and Young 2003). A consistent long-term altimeter dataset combining seven altimeter missions over the period 1995–2009 was develop by Zieger et al. (2009) and in the context of the Globwave dataset by Ash et al. (2010).

Consistent long-term radiometer and scatterometer datasets are described by Wentz (2013) using a combination of buoy data and cross validation between missions comparing the radiative transfer models for instruments. A 20-yr dataset was produced by Atlas et al. (2011) using a variational analysis method that combined cross-validated radiometer data from multiple satellites with in situ data and model results. We are not aware of any attempts to combine different types of instruments (e.g., altimeter and radiometer), as described here to create a single long-term dataset.

As will be noted later, one of the challenges in the calibration/validation of such datasets is that there is no true "ground truth." Buoy data, as used in this study, are often regarded as such, but they are associated with their own errors and limitations, particularly at extreme conditions. Approaches, such as triple collocation, have been proposed to account for the variety of error sources (Stoffelen 1998; Hoffman et al. 2013). The various calibration studies have demonstrated the accuracy of all the instruments considered here. Zieger et al. (2009) report RMS errors of less than 0.25 m for H_s and 1.7 m s^{-1} for U_{10} from altimeters, whereas Wentz (2013) reports an RMS U_{10} error of 0.9 m s^{-1} for radiometer data.

TABLE 1. Summary of all satellite instruments in the combined database. Duration of each satellite mission and σ_0 offset used to calculate U_{10} for altimeters are listed. Versions of the raw datasets sourced from Globwave or RSS are listed.

Mission	Dates	σ_0 offset (dB)	Instrument	Data source
Geosat	31 Mar 1985–30 Dec 1989	0.091	Altimeter	GW_L2P_ALT_GEOS_GDR
ERS-1	1 Aug 1991–2 Jun 1996	0.030	Altimeter	GW_L2P_ALT_ERS1_GDR
TOPEX	25 Sep 1992–8 Oct 2005	−0.697	Altimeter	GW_L2P_ALT_TOPX_GDR
ERS-2	29 Apr 1995–11 May 2009	−0.030	Altimeter	GW_L2P_ALT_ERS2_GDR
GFO	7 Jan 2000–7 Sep 2008	−0.394	Altimeter	GW_L2P_ALT_GFO_GDR
Jason-1	15 Jan 2002–3 Mar 2012	−3.214	Altimeter	GW_L2P_ALT_JAS1_GDR
Envisat	14 May 2002–8 Apr 2012	−0.152	Altimeter	GW_L2P_ALT_ENVI_GDR
Jason-2	22 Jun 2008–10 May 2012	−3.038	Altimeter	GW_L2P_ALT_JAS2_GDR
CryoSat	14 Jul 2010–1 Apr 2015	−0.212	Altimeter	GW_L2P_ALT_CRYO_GDR
SSM/I *F8*	9 Jul 1987–31 Dec 1991	—	Radiometer	REMSS V7
SSM/I *F10*	8 Dec 1990–14 Nov 1997	—	Radiometer	REMSS V7
SSM/I *F11*	3 Dec 1991–16 May 2000	—	Radiometer	REMSS V7
SSM/I *F13*	3May 1995–4 Nov 2009	—	Radiometer	REMSS V7
SSM/I *F14*	8 May 1997–8 Aug 2008	—	Radiometer	REMSS V7
SSM/I *F15*	18 Dec 1999–31 Dec 2011	—	Radiometer	REMSS V7
SSM/I *F16*	26 Oct 2003–28 May 2013	—	Radiometer	REMSS V7
SSM/I *F17*	14 Dec 2006–25 May 2013	—	Radiometer	REMSS V7
AMSR-E	1 Jun 2002–4 Oct 11	—	Radiometer	REMSS V7
AMSRJ	18 Jan 2003–24 Oct 2003	—	Radiometer	REMSS V5
TMI	6 Dec 1997–6 Jun 2013	—	Radiometer	REMSS V4
WindSat	5 Feb 2003–23 Jun 2013	—	Radiometer	REMSS V7
QuikSCAT	19 Jul 1999–19 Nov 2009	—	Scatterometer	REMSS V4
SeaWinds	10 Apr 2003–24 Oct 2003	—	Scatterometer	REMSS V3

3. Available data

One of the confusing and concerning elements of satellite oceanography is that the numerous calibrations of satellite data against buoys appear to yield a range of results. This is caused for a number of reasons, including the matchup criteria of time and position used to extract data (see below and section 6), the period of time over which the calibrated data has been considered, and the algorithm or version used to determine the geophysical quantity (H_s or U_{10}) from the quantity sensed by the satellite. All of these variables will be defined in some detail for the present analysis. In addition, all satellite data used in this study have been sourced from two publicly available archives, thus reducing the variability that may result from sourcing data from a large number of primary sources.

a. Altimeter data

The altimeter data was sourced from the public domain Globwave archive (http://globwave.ifremer.fr/). The data used were along-track LP2 data with the details provided in Table 1. The along-track LP2 data consist of 1-Hz data along the altimeter ground track. A total of nine altimeter missions were included in the full dataset: *Geosat*, *ERS-1*, TOPEX, *ERS-2*, *Geosat Follow-On* (*GFO*), *Jason-1*, *Envisat*, *Jason-2*, *CryoSat* (expressed in order of launch). These altimeter missions spanned the period from 31 March 1985 until 1 April 2015 and are shown in Fig. 1. This is a period of 30 years with a gap of 1 year and 8 months in 1991 and 1992 between the *Geosat* and *ERS-1* missions.

The values of H_s were taken directly from the Globwave netCDF files. However, following the approach used by Zieger et al. (2009), U_{10} was calculated from the Globwave values of σ_0 using the algorithm proposed by Abdalla (2007),

$$U_{10} = U_m + 1.4U_m^{0.096}\exp(-0.32U_m^{1.096}), \qquad (1)$$

where

$$U_m = \begin{cases} 46.5 - 3.6\sigma_0 & \text{for} \quad \sigma_0 \le 10.917\,\text{dB} \\ 1690\exp(-0.5\sigma_0) & \text{for} \quad \sigma_0 > 10.917\,\text{dB} \end{cases}.$$

In (1), U_{10} is in meters per second and σ_0 is in decibels. This approach was adopted to ensure a consistent algorithm was used across all altimeter platforms.

At each matchup point between buoy wind speed, corrected for anemometer height, and altimeter, σ_0 was extracted (see section 4). As demonstrated by Zieger et al. (2009), an altimeter-specific σ_0 offset needs to be applied to each altimeter dataset before the Abdalla (2007) relationship can be applied. The σ_0 offset was determined to yield the minimum least squares difference between the Abdalla (2007) function and the U_{10} (buoy)–σ_0 (altimeter) data. The resulting σ_0 offset values are shown in Table 1. The σ_0 offset for most instruments is relatively small. However, for *Jason-1* and *Jason-2*, it is

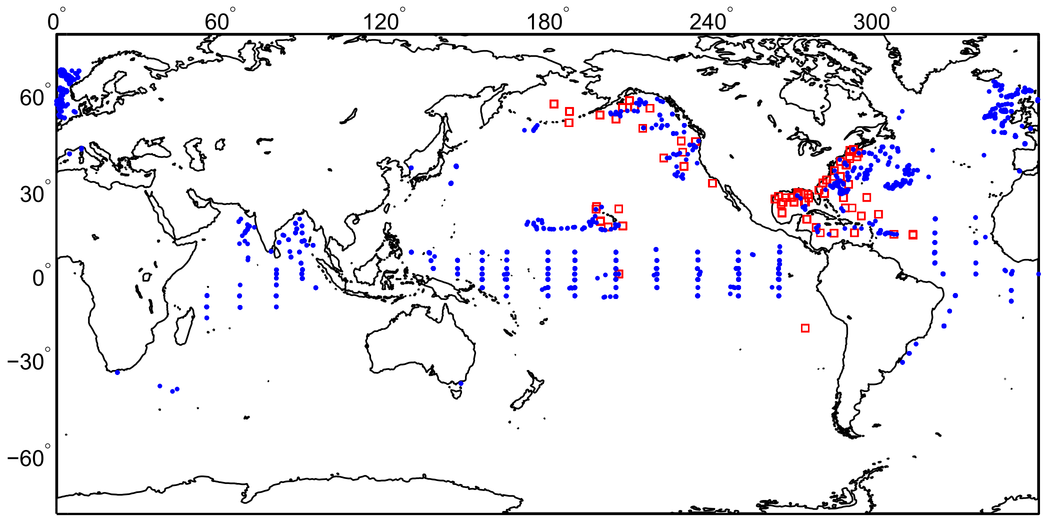

FIG. 2. Locations of buoys used for the calibration and validation of the satellite systems: NDBC buoys (red squares) and ECMWF combined buoys (blue dots).

approximately 3 dB. The reason for this large offset is not clear and appears to be unique to the versions of the data in the Globwave database, as such large offsets were not found by Zieger et al. (2009). Once this offset is applied, however, all other aspects of the *Jason-1* and *Jason-2* wind speed data appear consistent with buoy measurements and other altimeters. That such offsets are needed reflects the fact that functions such as (1) are developed only for a specific subset of satellites and for use with particular versions of the satellite products. As noted earlier, care needs to be exercised to ensure the particular set of data under consideration is calibrated consistently before being used.

b. *Radiometer and scatterometer data*

The radiometer and scatterometer data were sourced from the public domain Remote Sensing Systems (REMSS) archive (http://www.remss.com/). The data used were the daily gridded fields, which provide data along the satellite track and across the swatch at 25-km resolution. A total of 12 radiometers were included in the dataset: SSM/I *F8–F17*, AMSR-E, AMSRJ, TMI, and WindSat. These missions span a period of 26 years from July 1987 to June 2013. Two scatterometer missions were also included: QuikSCAT and SeaWinds, which span a period of 10 years from July 1999 to November 2009. Wind speed values U_{10} and wind direction θ_w (for scatterometer) were taken directly from the REMSS data files.

c. *In situ buoy data*

To adequately calibrate and assess the long-term stability of the satellite dataset, it is desirable to have a high-quality in situ buoy dataset covering the full 30 years of satellite data with a broad geographic distribution. The best known and most commonly used buoy dataset is the NDBC archive (Evans et al. 2003). Although the NDBC dataset covers the full period of the satellite database, it is geographically limited to areas around the continental United States and Hawaii. The NDBC data are generally regarded as high quality, although questions have been raised about its long-term consistency (Gemmrich et al. 2011; Jensen et al. 2015). As a result, a second independent buoy dataset was also utilized. The European Centre for Medium-Range Weather Forecasts (2014, personal communication) provided access to its combined buoy dataset. This dataset contains data sourced from a range of different agencies, including the Met Office, Météo-France, the French Naval Hydrographic and Oceanographic Service [Service hydrographique et océanographique de la Marine (SHOM)], the Marine Environmental Data Service (MEDS; Canada) and TAO/TRITON (tropical data). This combined ECMWF dataset significantly enhances the geographic spread of the data, but as it originates from a large range of sources, ensuring consistent analysis and recording processes is problematic. Therefore, the NDBC dataset has been used as the primary source for calibration of the satellite database, with the combined ECMWF dataset used as an independent validation for results. The locations of all buoys in both the NDBC and composite ECMWF databases are shown in Fig. 2.

The vast majority of the buoys in both networks measure hourly values of either H_s, U_z, or both, where U_z is the wind speed at the height of the anemometer z. The wind speed at a standard reference height of 10 m was determined assuming a logarithmic boundary layer profile (Young 1999),

$$U_{10} = U_z \sqrt{\frac{\kappa^2}{C_d}} \frac{1}{\ln(z/z_0)}, \tag{2}$$

where κ is the von Kármán constant ≈ 0.4 and C_d is the drag coefficient. Measurements of C_d over the ocean yield results with scatter of an order of magnitude, and much research has focused on the wind speed and sea state dependence of C_d (e.g., Donelan 1982; Young 1999; Guan and Xie 2004). Noting the inherent difficulties in accurately measuring wind speed from a floating buoy (e.g., Bender et al. 2010), a representative constant value of $C_d = 1.2 \times 10^{-3}$ was adopted. This value is consistent with the recommendations of Guan and Xie (2004) and the wind speed–dependent relationship of Donelan (1982), $C_d = (0.96 + 0.041U_{10}) \times 10^{-3}$, assuming a typical mean oceanic wind speed of $U_{10} = 5\,\mathrm{m\,s^{-1}}$. With $C_d = 1.2 \times 10^{-3}$ and $z = 10\,\mathrm{m}$, (2) yields $z_0 = 9.7 \times 10^{-5}\,\mathrm{m}$. A range of tests was conducted with constant wind speed–dependent and sea state–dependent values of C_d. These different assumptions had little impact on the final satellite wind speed calibrations. A fuller investigation of the potential errors associated with the determination of U_{10} from buoy anemometer measurements can be found in section 6.

4. Calibration against buoy data

a. Altimeter calibration

The altimeter and buoy datasets were searched for "matchups," where the altimeter track was within 50 km of a buoy and the overpass occurred within 30 min of the buoy recording data. These matchup criteria were consistent with that adopted by Dobson et al. (1987), Monaldo (1988), Gower (1996), Queffeulou (2003, 2004), Queffeulou et al. (2004), and Zieger et al. (2009). A range of values for both spatial and temporal mismatches was tested and this combination seemed an optimal choice. It produced a sufficient number of collocations for a stable result while ensuring both buoy and altimeter responded to the same approximate wind/wave field (see section 6). Only buoys located more than 50 km offshore were considered, so as to avoid nearshore impacts on both buoy and satellite data (see section 6). A range of additional quality control criteria was set:

- A minimum of five points were required in the altimeter pass within the 50-km radius region around the buoy.
- Cases where there was large along-track variability in the altimeter data were excluded. Passes for which $\sigma(H_s)/\overline{H}_s > 0.2$ were excluded, where $\sigma(H_s)$ and $\overline{H}_s$ are the standard deviation and mean of values of H_s along the altimeter subtrack, respectively. The same criteria were also applied for wind speed U_{10}.
- The Globwave altimeter files contain a quality flag, swh_qcl. Only data with swh_qcl = 0, indicating "good" data were retained.

The implicit assumption in calibration against buoy data is that the buoy data are the ground truth. In reality, both wind speed and wave height measurements from buoys are subject to both sampling and instrumental errors. Buoy values of H_s are usually obtained from spectral analysis of 20-min records and wind speed from a 10-min mean. As such, each of these estimates represent one realization of the true value (Bendat and Piersol 1971; Young 1986) and are subject to statistical sampling errors. In addition, the accelerometers that are used to measure wave height and the anemometers that measure wind speed are subject to instrumental accuracy. Finally, most of the in situ measurements are obtained from floating buoys. The motion of the buoys, the sheltering provided by large waves in extreme sea states, and the mooring systems all limit the accuracy of the in situ measurements (Large et al. 1995; Zeng and Brown 1998; Taylor and Yelland 2001; Howden et al. 2008; Bender et al. 2010; Jensen et al. 2015). Section 6 provides an analysis of the potential impacts on wind speed measurements. Therefore, both satellite and buoy data contain errors. This situation can be accommodated, to some extent, by the use of reduced major axis (RMA) regression (Trauth 2007). RMA regression minimizes the triangular area bounded by the x and y axes and the cord of the regression line. This contrasts with conventional regression that minimizes the y offset from the regression line. Standard least squares regression analysis is highly sensitive to outliers. Such outliers can be removed by the use of robust regression (Holland and Welsch 1977). Robust regression assigns a weight to each point, with values between 0 and 1. Points with a value less than 0.01 were designated as outliers and removed from the analysis before applying the RMA regression analysis.

The matchup data for each of the altimeter missions were used to carry out the RMA regression calibration against the NDBC buoy dataset. The results for these calibrations appear in Table A1, with examples of the resulting scatterplots shown in Fig. 3. Figure 3 clearly shows that there is less scatter in the matchup plots for H_s than for U_{10}, supporting the common view that the altimeter has greater precision when measuring wave height than wind speed. This probably occurs for two reasons. First, wind by its nature is more spatially variant

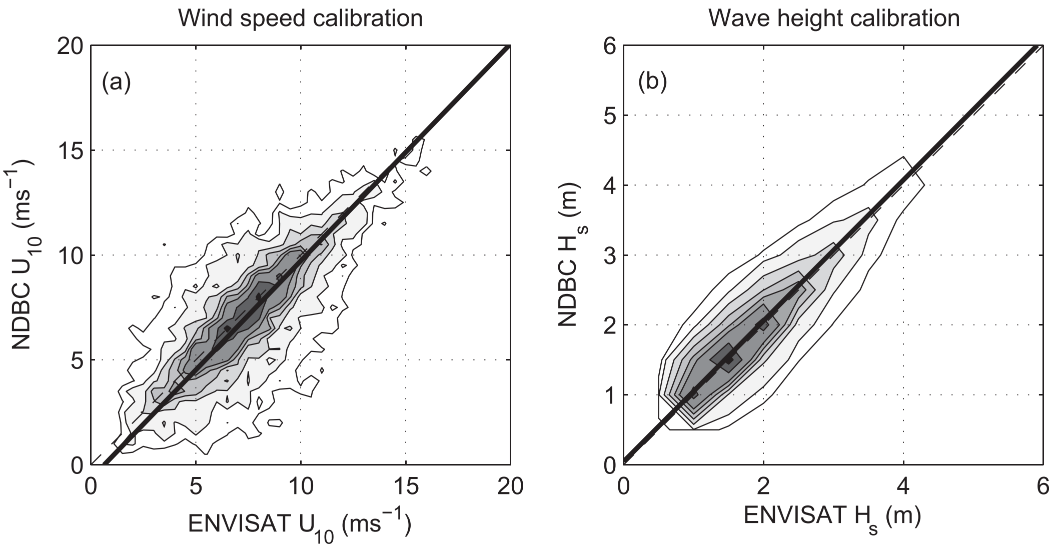

FIG. 3. Calibration of *Envisat* altimeter against NDBC buoy data: (a) wind speed and (b) significant wave height. Shown are the 1:1 agreement (dashed diagonal line) and the RMA regression (thick solid line). Contours show the density of matchup data points. The density of values has been normalized such that the maximum value is 1.0. Contours are drawn at 0.9, 0.8, 0.7, . . . , 0.1, 0.05.

than wave height. There can be rapid spatial variations, including fronts in a wind field. In contrast, wave fields are dispersive and vary smoothly in space. Hence, the spatial and temporal mismatch between altimeter and buoy will be larger for wind speed measurements than for wave height measurements. Second, the imaging mechanism for wind speed is less direct than for wave height. The wind speed is determined from the radar backscatter, which is influenced by high-frequency waves generated by the wind. In addition, contaminates on the water surface, such as the presence of biological or chemical slicks, can impact the radar backscatter (Qi and Zhao 2015). The presence of surface currents can also influence the surface stress, which will impact values of U_{10} obtained by satellites.

To assess the quality of the RMA fit to the data, Table A1 also includes the 95% confidence limits on both the slope and offset for the regression, using the approach of Ricker (1973). A more detailed Monte Carlo analysis of the confidence limits appears in section 6.

As noted above, a comparison of the results with previous studies is difficult, as the durations of the data comparisons and the precise version numbers of the altimeter product vary. However, Ash et al. (2010) have undertaken a similar analysis for Globwave altimeter H_s to the data reported in Table A1. Although the duration for which data are considered for each satellite varies, compared to the present analysis the results are very similar. The slope of the regression line differs by at most 3% for any of the altimeters (Ash et al. 2010; do not consider *Geosat* or *CryoSat*). The NDBC calibration results for H_s are also consistent with the ECMWF composite buoy dataset (Table A2); however, the slope of the regression line is lower for every altimeter with the exception of *CryoSat* by an average of 5%. This may be because the datasets cover different geographic regions, with the ECMWF dataset containing European data and significantly more equatorial data. However, it appears more likely that the ECMWF H_s values are, on average, lower than the NDBC dataset. Durrant et al. (2009) undertook a similar analysis using *Jason-1* and *Envisat* as references and reported that the Canadian MEDS buoys measure H_s on average 10% lower than NDBC buoys. The present ECMWF dataset includes the MEDS buoys and hence the 5% underestimation seen in the present data is consistent with Durrant et al. (2009).

The calibrations for altimeter U_{10} are also consistent across the NDBC and ECMWF datasets. Again, the ECMWF data appear to be approximately 4% lower than the NDBC data. However, this is largely driven by *CryoSat*, where the ECMWF comparison is 12% lower than NDBC. If *CryoSat* is removed, then the ECMWF data are only 1.5% lower than NDBC. The reason for the difference in *CryoSat* is not obvious. As a relatively new instrument, its long-term performance is still not extensively investigated.

The calibrations reported in Tables A1 and A2 and shown in Fig. 3 contain data from the full duration of each altimeter mission. As pointed out by Zieger et al. (2009), it is important to also understand the long-term stability of the data. Such an analysis can reveal any step changes in calibration that might occur due to changes in satellite

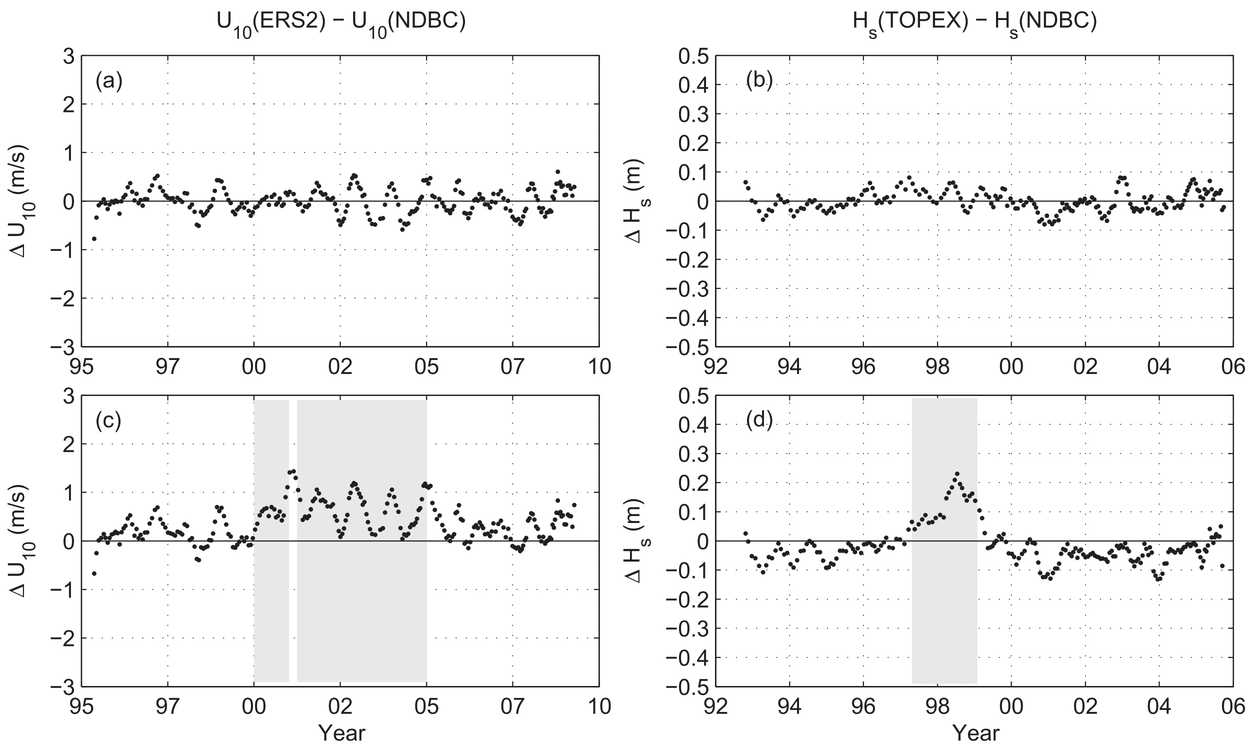

FIG. 4. Difference between altimeter and NDBC buoy values of U_{10} and H_s as a function of time. The ERS2 altimeter is shown in panels (a) and (c) and the TOPEX altimeter in panels (b) and (d). Panels (c) and (d) show the result when a single calibration relation is used over the full period of the mission (i.e. Table A1). Regions where there were either discontinuities (c) or drift (d) are shown by shading. Panels (a) and (b) show the result when piecewise calibration was used (i.e., Table A3).

systems or data processing or any drift in the calibration with time. The quantities $\Delta H_s = H_s(\text{alt}) - H_s(\text{buoy})$ and $\Delta U_{10} = U_{10}(\text{alt}) - U_{10}(\text{buoy})$, where the terms in parentheses refer to the altimeter and buoy, respectively, were calculated at each matchup and plotted as a function of time. To remove some of the temporal variability, the results were block averaged with nonoverlapping blocks of 40 points. Examples of typical results are shown in Fig. 4.

Figure 4d shows TOPEX ΔH_s. The clear drift that occurs between 1997 and 1999 has been previously reported by a number of authors (e.g., Dorandeu 1999; Zieger et al. 2009). Figure 4c shows *ERS-2* U_{10}, where there appears to be a step change in ΔU_{10} in the period from 1 January 2001 to 1 June 2005. Across all satellite missions, only two examples of drift were apparent: the TOPEX H_s drift noted above and a drift in GFO U_{10} that commenced around 1 March 2006 and continued until the end of the mission in 2008. These occurrences of drift were removed by fitting a function to the period of the drift and subtracting this from the data (details of functions shown in Table A3). In cases where there were discontinuities or step changes in the data, as in Fig. 4c, the data were partitioned either side of the discontinuity and separate calibrations were carried out for each segment (called ‘‘partial calibration’’). The positions of such discontinuities were first determined from the NDBC data and then confirmed with the ECMWF data. There was strong correlation between the two datasets. These results were then also confirmed from altimeter–altimeter matchups (see section 5). The final partial calibrations for both wind speed and wave height are given in Table A3 (for NDBC). Figures 4a and 4b are the same as Figs. 4c and 4d, respectively, but after the drift and discontinues have been removed using the partial calibration process.

Calibration results, such as those shown in Fig. 3, indicate good agreement between altimeter and buoy over the full range of buoy measurements of H_s and U_{10}. However, the calibration functions, shown in Tables A1 and A3 are weighted toward the bulk of the data at moderate values of wind speed and wave height. A better understanding of the performance of the altimeter across the full range of values can be obtained by comparing the probability distribution functions (pdf) for altimeter and buoy. This can be done with the use of quantile–quantile (Q–Q) plots. This was done for all altimeters for both H_s and U_{10} and for both buoy datasets (NDBC and ECMWF). In all cases the Q–Q plots were in good agreement across the full range of

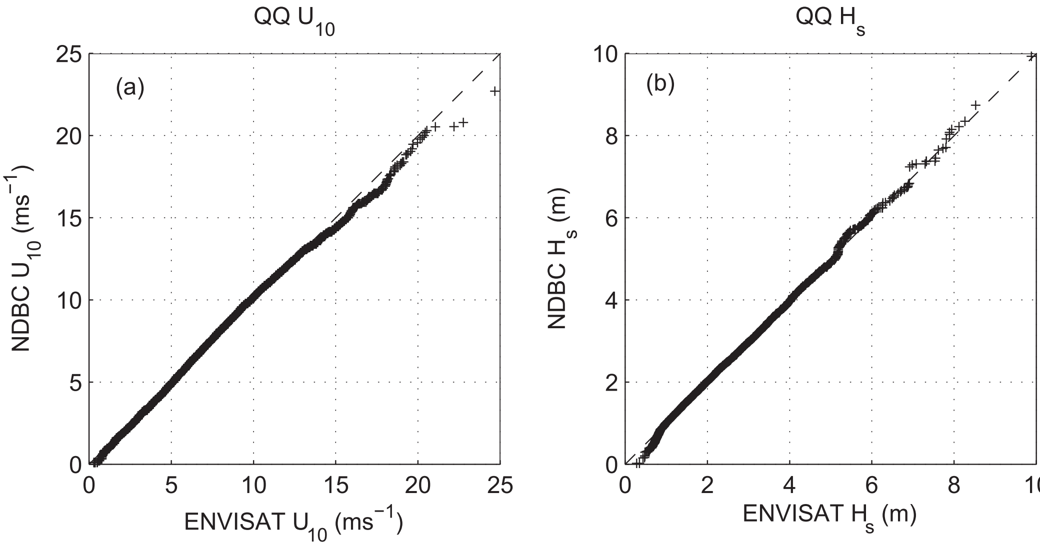

FIG. 5. Q–Q plots between the *Envisat* altimeter and NDBC buoy data. Shown are (a) wind speed and (b) significant wave height.

available data. Figure 5 shows the Q–Q plots for *Envisat*–buoy for both H_s and U_{10}. Figure 5a suggests that *Envisat* may produce slightly higher wind speeds than the buoys at high values of U_{10}. *GFO* showed a similar tendency, although in neither case is this entirely clear, as there are little data above $20\,\mathrm{m\,s^{-1}}$. This behavior was not present in any of other altimeters, which showed good agreement between the probability distribution functions out to values of $25\,\mathrm{m\,s^{-1}}$. This agreement does, however, raise the question of whether floating buoys can accurately measure wind speed and wave height under extreme conditions, as noted above. This is examined in more detail in section 6.

The performance of altimeter-derived wind speed and wave height at extreme value is particularly important for many engineering applications and, although the good agreement between altimeter and buoy pdfs is encouraging, the lack of confidence in the ability of buoys to accurately measure such condition raises doubts about the use of such altimeter data to predict extreme conditions. If, for instance, buoys underestimate high wind speed and wave height (Large et al. 1995; Zeng and Brown 1998; Taylor and Yelland 2001; Howden et al. 2008; Bender et al. 2010; Jensen et al. 2015), then the abovementioned results indicate that altimeter extreme values ($U_{10} > 15\,\mathrm{m\,s^{-1}}, H_s > 7\,\mathrm{m}$) may also be underestimated. In addition to issues around buoy accuracy, the $\sigma_0 - U_{10}$ relationship for the altimeter becomes less sensitive at high wind speeds and questions over the accuracy of altimeter wind speed measurements at high wind speeds have been raised (e.g., Young 1993). Young et al. (2011) also raised concerns about the accuracy of *Geosat* U_{10} at high wind speeds. The present results indicate that *Geosat* performance at high wind speeds is comparable to the other altimeter missions.

b. Radiometer and scatterometer calibration

The same matchup criteria were applied to the radiometer/scatterometer data as for altimeter., that is, a collocation separation of 50 km and 30 min (see section 6). In addition, there needs to be a minimum of five points in the satellite pass and only points that have a ''no rain'' flag and a ''good quality'' flag set were retained. All points in the pass that met these criteria were averaged to obtain a representative radiometer/scatterometer U_{10} to be compared to the buoy wind speed, corrected for anemometer height as in section 3c. As for the altimeters, only buoys greater than 50 km offshore were considered (see section 6). The RMA analysis was then applied as for altimeter data.

Figure 6 shows typical examples of the analysis for the SSM/I *F13* radiometer (Fig. 6a) and the QSCAT scatterometer (Fig. 6b). The full RMA analysis results appear in Tables A4 and A5. Table A4 shows the calibration against the NDBC dataset and Table A5 shows the validation against the ECMWF composite dataset. In contrast to the altimeters, where the calibrations differed significantly between the instruments, all of the SSM/I instruments have very similar calibration results. This is not surprising, as the REMSS wind speed relationships were developed by intercomparison between the SSM/I instruments, rather than by the calibration of

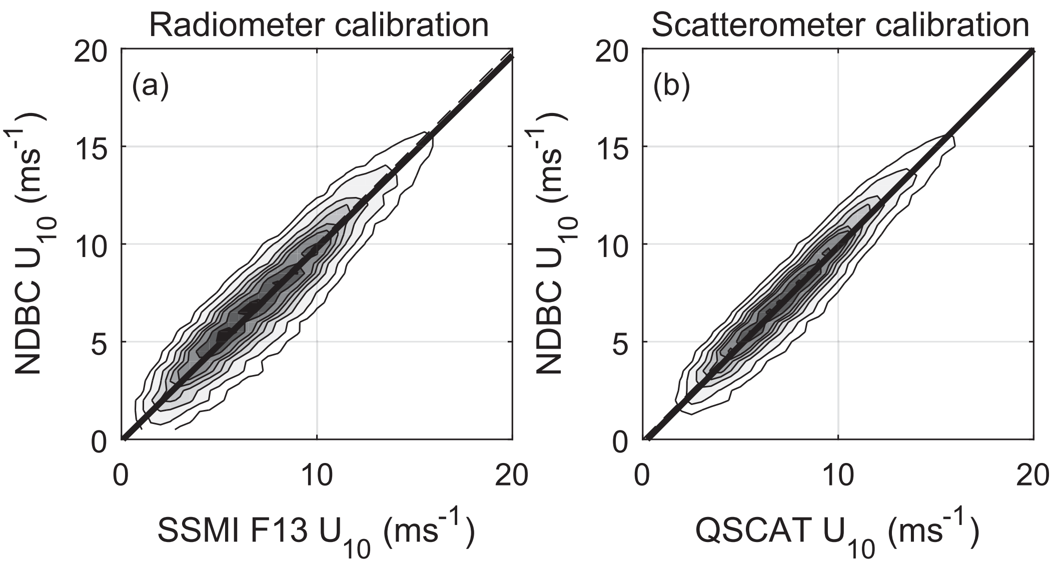

FIG. 6. Calibration of (a) SSM/I *F13* radiometer wind speed against NDBC buoy data and (b) QSCAT scatterometer wind speed against NDBC buoy data. Shown are the 1:1 agreement (dashed diagonal line) and the RMA regression (thick solid line). Contours show the density of matchup data points. The density of values has been normalized such that the maximum value is 1.0. Contours are drawn at 0.9, 0.8, 0.7, . . . , 0.1, 0.05.

individual instruments against buoys (Wentz 2013). With the exception of the TMI radiometers, the validation against the ECMWF buoy data is consistent with the altimeter results and indicated that the ECMWF dataset is, on average, 1% lower than the NDBC data.

The results shown in Tables A4 and A5 indicate, on average, a small negative U_{10} offset compared to the REMSS values (i.e., buoys less than REMSS). For a typical global average wind speed of $U_{10} = 7.5$ m s^{-1}, the results in Tables A4 and A5 give average (averaged across all satellites) offsets of -0.220 m s^{-1} (-2.9%) for the NDBC buoys and -0.319 m s^{-1} (-4.2%) for the ECMWF buoys. This offset varies across the satellites. For the NDBC buoys, it has a maximum of -0.388 m s^{-1} (-5.2%) for SSM/I *F10* and a minimum of -0.088 m s^{-1} (-1.2%) for AMSR-E–MF. For the ECMWF buoys, the offset has a maximum of -0.445 m s^{-1} (-5.9%) for WindSat and a minimum of -0.112 m s^{-1} (-1.6%) for TMI–LF. The fact that there is a consistently negative offset (although magnitude varies) compared to the REMSS values, which used a similar set of calibration buoys, suggests that the explanation for these differences may lie in the selection of buoys or the treatment of the buoy wind speed measurements. The fact that the relative magnitudes of the offsets for individual satellites vary between the NDBC and ECMWF datasets (i.e., the maximum and minimum values are for different satellites) suggest that these small differences may represent the limitations of buoy accuracy. These possibilities are examined in more detail in section 6. Compared to the altimeter wind speeds, however, the REMSS radiometer winds represent a consistent dataset in good agreement with buoy data.

As with the altimeter data, the radiometer/scatterometer U_{10} was also checked for long-term stability by determining $\Delta U_{10} = U_{10}(\text{rad}) - U_{10}(\text{buoy})$ as a function of time, where $U_{10}(\text{rad})$ is the radiometer/scatterometer wind speed. Figure 7 shows examples of these relations as a function of time for the TMI radiometer (MF band) (Fig. 7a) and the QSCAT scatterometer (Fig. 7b). The results for all radiometers/scatterometers were stable as a function of time with no indications of drift or discontinuities. This is perhaps not surprising, as the REMSS calibration process uses intercomparisons of satellite missions as a key element of the approach. Hence, a single calibration for each mission, as shown in Table A4, is appropriate for all the radiometer/scatterometer missions. If one assumes that the initial REMSS intersatellite calibrations minimized the differences between satellite missions, then the individual buoy-related relations in Tables A4 and A5 will introduce some inconsistency between the satellites. However, the results in Tables A4 and A5 do minimize the differences with the present buoy datasets (see section 7).

A clear periodicity of 1 year is evident in Fig. 7 with ΔU_{10} reaching a maximum in January and a minimum in June/July. This same feature was also apparent in

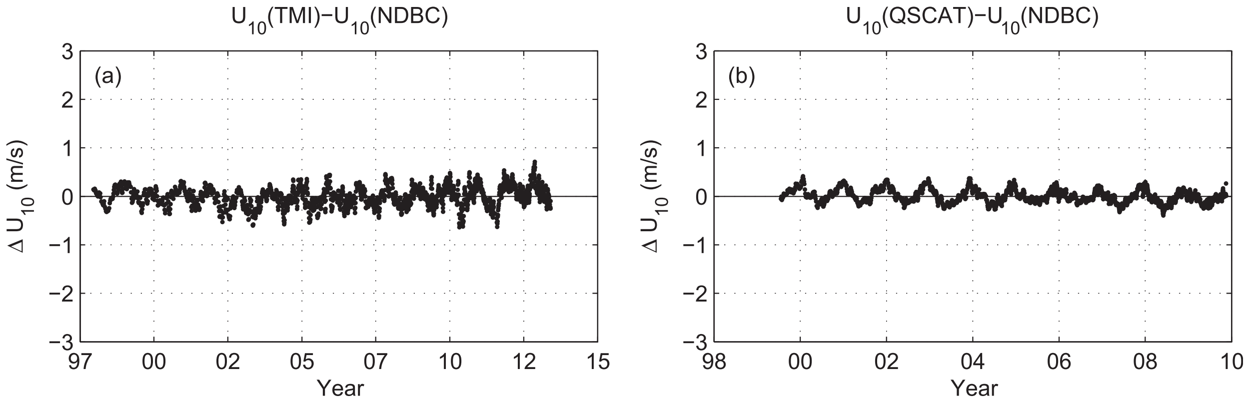

FIG. 7. Differences between (a) TMI radiometer (MF band) and NDBC buoy wind speed as a function of time and (b) QuikSCAT scatterometer and NDBC buoy wind speed as a function of time.

altimeter ΔU_{10} and to some extent ΔH_s in Fig. 4. In assessing the reason for this seasonal oscillation, it is important to note that the vast majority of the NDBC buoys are at latitudes greater than +30°. January corresponds to the Northern Hemisphere winter, when both wind speed and wave height are a maximum for these latitudes. Although the oscillations are clear in the ΔU_{10} time series, the amplitude of the oscillations are relatively small, typically of order 0.3 m s^{-1}. Typical climatologies for the North Pacific and North Atlantic indicate mean monthly wind speeds for January of approximately 12 m s^{-1} (e.g., Young 1999); that is, the oscillations are approximately 3% of the mean condition.

There are two likely causes for these oscillations. The first is the influence of atmospheric stability on the boundary layer (Large and Pond 1982; Young 1998a). Under neutral conditions, when the air and water temperatures are equal, there is a logarithmic boundary layer in the air. If the water is warmer than the air (unstable conditions), there will be an upward flux of heat and more dense air will overlay less dense air. The result is a more uniform distribution of velocity in the boundary layer than under neutral conditions. Unless accounted for, this will impact the estimates of U_{10}. It will also impact the shear stress on the water surface that the altimeter, radiometer, and scatterometer all indirectly rely upon to determine U_{10}. During winter (i.e., January in the Northern Hemisphere) the air temperature will often be less than the water temperature and unstable conditions will not be uncommon. Hence, it is not surprising that a seasonal signal exists in the wind speed difference for all instruments. Mears et al. (2001) reported similar stability-related impacts for buoy–radiometer comparisons.

Atmospheric stability also has an influence on wave height. Young (1998a) has shown that the changes to the atmospheric boundary layer changes the generation of waves and results in enhanced wave growth rates under unstable conditions. However, it is unlikely that this mechanism would result in a seasonal signal in ΔH_s. The altimeter measures H_s from the shape of the return altimeter pulse (see section 2a), which is directly influenced by the average height of the waves over the altimeter footprint. The changed shape of the boundary layer may change the wave spectrum in some manner (e.g., the relationship between height and period), but this is likely to have a small impact on the altimeter measurements of H_s. However, the seasonal oscillation in altimeter ΔH_s was much less clear than for ΔU_{10}. *Envisat*, *Jason-1*, and TOPEX show some evidence of the oscillation; the other five altimeters do not show this phenomenon.

The second possible cause for the seasonal oscillation is that there is a small mismatch between the calibrated altimeter/radiometer/scatterometer data and the buoy data. Moving from summer to winter results in the wind speed/wave height seasonally increasing and decreasing. This is the same as moving up and down the diagonal line on Figs. 3 and 6. If the data cloud is not perfectly distributed around the calibration line, then this will result in an average mismatch between buoy and satellite data that will also vary seasonally. The absolute error is likely to be larger during larger winds/waves and smaller during smaller wind/waves. Although the calibration relations were developed using RMA regression to best fit the buoy data, they were developed for aggregate data from the whole NDBC dataset. Had, for instance, only buoys with a latitude north of +30° been consider, the resulting RMA regression would have been different. Tests with different subsets of buoys showed that a difference of 2%–3% could easily result in these circumstances (see section 6).

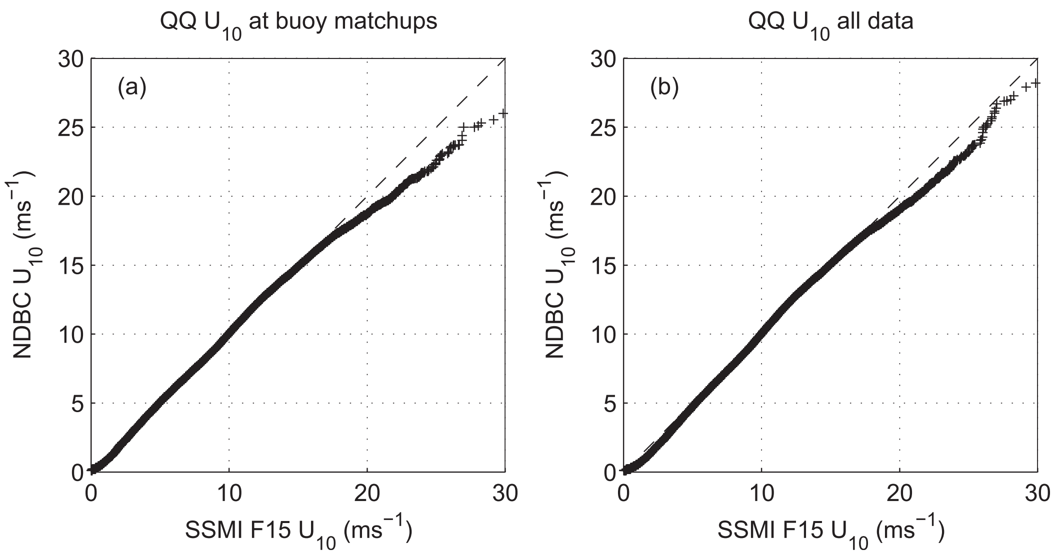

FIG. 8. Q–Q plots between SSM/I *F15* and NDBC buoy wind speeds. (a) Case where there is a 1:1 correspondence between data points. (b) Case where there is a matchup between data points but *SSM/I F15* points with a rain flag set are excluded. Difference between the panels is caused by the fair weather bias in the radiometer data.

Separating the two influences is difficult, as both have the same phase and frequency. Presenting ΔU_{10} and ΔH_s in nondimensional form (i.e., $\Delta U_{10}/U_{10}$) was investigated as an alternative presentation. Although this might address the issue of calibration mismatch as a function of the absolute magnitude, it will not address any atmospheric stability issues. Alternative presentations of this form proved inconclusive. Tests were also performed where the calibration relations were systematically increased/decreased at large values of U_{10} and H_s in an attempt to investigate the sensitivity to a calibration mismatch. Through this process it was possible to reduce the magnitude of the oscillations for ΔH_s but ΔU_{10} was not significantly impacted.

Data from a deep-water buoy at an equivalent Southern Hemisphere location would help to resolve this issue. However, there is very little such long-term data available. One possibility is the Southern Ocean Flux Station (SOFS) (Rapizo et al. 2015) buoy located at latitude −46.7°, south of Australia in the Southern Ocean. The full deployment covers a period of approximately 3.5 years (March 2010–October 2013), but the total duration of data is only approximately 700 days with two large data gaps of many months when the buoy was serviced. This data record was investigated but found to be too short and fragmented to be able to be analyzed for a periodic signature in ΔU_{10}.

Without further data, we speculate that the oscillations are largely the seasonal response to atmospheric stability (Mears et al. 2001). The fact that this can be clearly seen in the data when it is only a few percent of the mean shows the quality and volume of the present dataset.

The shape of the radiometer/scatterometer pdf compared to the buoy dataset was investigated using Q–Q plots. Typical examples for both radiometer and scatterometer are shown in Fig. 8. Figure 8a shows the result where only ''matched'' data are considered; that is, for every buoy data point there is a matching radiometer/scatterometer data point. These are the same data used in developing the RMA calibrations (Table A4; Fig. 7). As noted above, radiometer/scatterometer data during heavy rain are unreliable. Hence, the data in Fig. 8a exclude such data from both the buoy and satellite records. However, a Q–Q plot does not require this one-to-one matchup of data. Figure 8b includes all data where there was a spatial and temporal matchup of buoy and satellite. That is, the buoy data include points for which the ''rain flag'' was set for the radiometer/scatterometer. As before, the radiometer/scatterometer excludes these data.

The results in Fig. 8 are typical of the Q–Q plots for all of the radiometer/scatterometer instruments when compared with both buoy datasets. Above approximately $20\,\mathrm{m\,s^{-1}}$, the ''matched up'' radiometer/scatterometer data have a greater percentage of the data in the tail of the pdf (Fig. 8a) than the buoy data. This is shown by the data falling below the diagonal line in the figure. This indicates there is a tendency for these instruments to record higher values of U_{10} than buoys at high wind speeds. As noted, above, buoy wind speeds are potentially biased low at higher wind speeds. Hence, the REMSS analysis potentially corrects for this feature. The magnitude of this correction is further investigated in section 6.

It could be assumed that since the radiometer/scatterometer data cannot measure during heavy rain, that this would introduce a ''fair weather'' bias. As strong winds in storms are often associated with rain, it is reasonable to assume that there would be less high wind data in the tail of the radiometer pdf as a result. Figure 8b addresses this issue by including ''rain'' data for the buoy but excluding these data from the radiometer/scatterometer data. This results in a reduction in the amount of data in the tail of the radiometer pdf, which elevates the Q–Q plot compared to Fig. 8a. That is, there is a fair weather bias in radiometer/scatterometer data, which means that these instruments miss some high wind cases due to heavy rain.

5. Cross validation between satellites

A further check on the consistency and stability of the various satellite instruments can be made by cross validation between the missions. The same criteria as used for the calibrations against buoys were used to extract matchup points between altimeter–altimeter and altimeter–radiometer/scatterometer missions. There are numerous such combinations of satellite missions (18 altimeter–altimeter and 49 altimeter–radiometer/scatterometer). In addition, the number of such collocated matchups is large when radiometer/scatterometer data are involved because of the width of the ground track swath. As a result, the search process to extract matchups was lengthy and in many cases the resulting matchup datasets have more than 250 000 points. All of the matchups for these various combinations were extracted and analyzed as above. That is, RMA validations were performed for each of the combinations, as well as for the investigation of the difference between the satellite H_s and U_{10} values as a function of time. Q–Q plots were also analyzed for each combination.

Figure 9 shows representative samples of RMA cross-validation results. Figures 9a and 9b show examples of RMA cross validation of wind speed between altimeter and radiometer and altimeter and scatterometer, respectively. As both instruments have been calibrated against buoy data, one would expect the cross-validation data to agree well. This was the case for all combinations of altimeter/radiometer/scatterometer. The maximum deviation in the slope of the RMA regression was 3%. As noted earlier, and in section 6, this magnitude of difference could be expected simply because this is an independent set of data to the NDBC buoy calibration dataset. Figures 9c and 9d show altimeter–altimeter cross validations for wind speed and Figs. 9e and 9f for significant wave height. Again, all cross validations between altimeters were in good agreement with the buoy calibrations (maximum difference of 3% in the slope of RMA regression).

Figures 9c–f show two different altimeter–altimeter combinations: *Jason-1*–*GFO* (Figs. 9c and 9e) and *Jason-1* –TOPEX (Figs. 9d and 9f). *Jason-1* and *GFO* are in different orbits and hence matchups generally occur when the satellite ground tracks cross at significant angles. In contrast, *Jason-1* and TOPEX are in the same orbit. They follow the same ground track with a time difference of less than 30 min to meet the selected matchup criteria. It is clear that when the satellites are in the same ground track, the scatter in the figures is very significantly reduced (Figs. 9d and 9f compared to Figs. 9c and 9e). This suggests that the scatter apparent in all of the results is largely due to the requirement to set a range of spatial and temporal matchup criteria rather than the inherent accuracy of the instruments.

Figure 10 show examples of Q–Q plots for a representative altimeter–radiometer wind speed combination (*Jason-1*–SSM/I *F15*). Two cases are shown in Fig. 10. The first (dashed–dotted line) is for the case of all matchup points. That is, there needs to be a unique matchup between radiometer and altimeter, with good data from both instruments (similar to Fig. 8b). Hence, this result will not show any ''fair weather'' bias in the radiometer data. Noting this, the altimeter produces lower estimates of wind speed than the altimeter above $U_{10} = 20\,\mathrm{m\,s^{-1}}$. These results are consistent with the buoy matchup Q–Q plots. Compared to the REMSS radiometer/scatterometer data, the altimeter underestimates the wind speeds at higher values of U_{10}. The performance of the REMSS radiometer data at high wind speeds is further investigated in section 6. Note also that Fig. 10 goes out to higher wind speeds than the buoy comparisons in Fig. 5b, as there are many more matchups for the radiometer–altimeter cases.

Figure 10 also shows *Jason-1*–SSM/I *F15* Q–Q results for a region rather than for exact matchups (''+'' symbols). All data for each instrument for a 1° × 1° square centered at +45.5°, 180.5° (North Pacific) and the duration of the *Jason-1* mission are considered (i.e., there does not need to be a unique matchup). This comparison was included to investigate whether

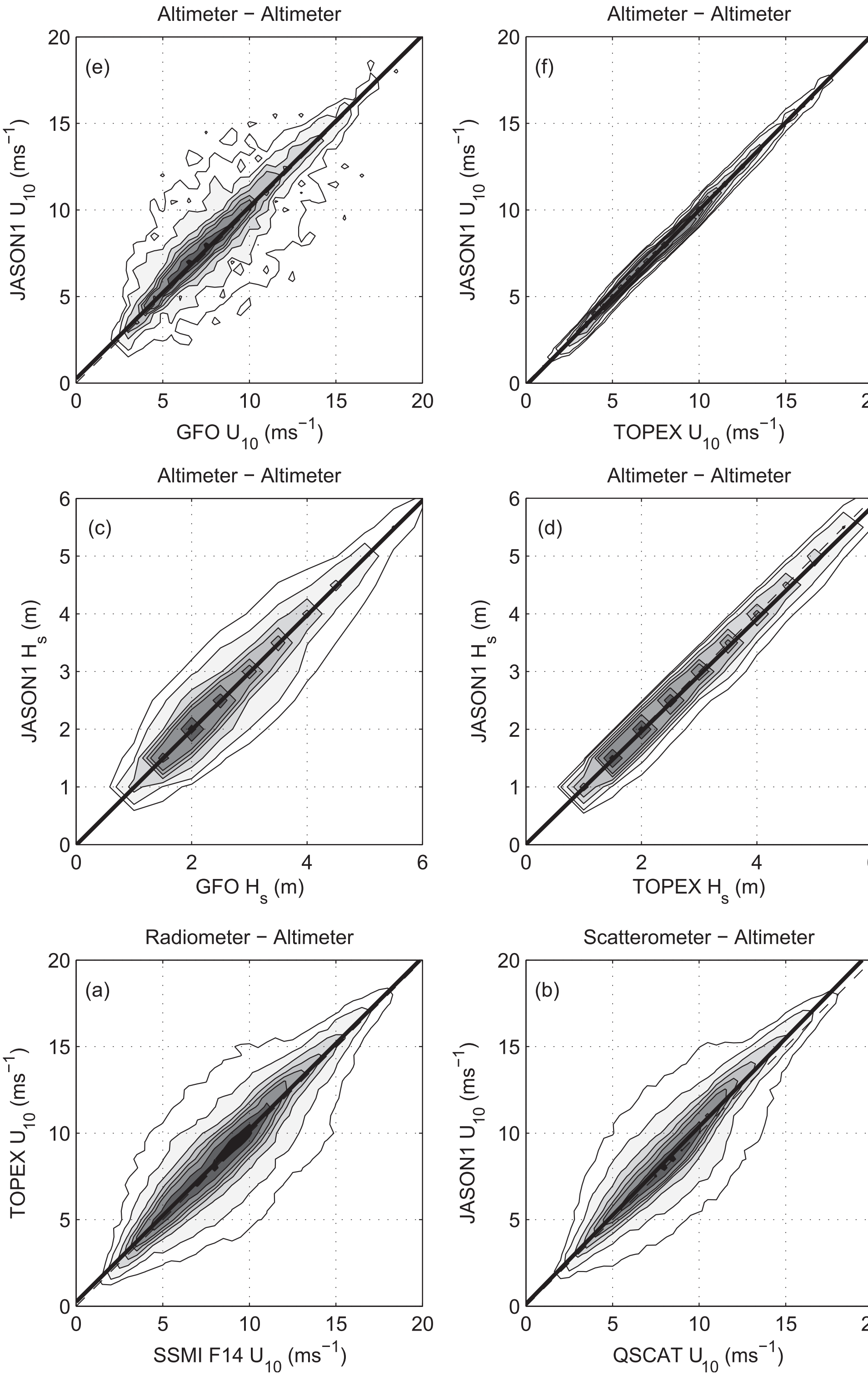

FIG. 9. Cross-validation matchup plots for the satellite sensors. Shown are the 1:1 agreement (dashed diagonal line) and the RMA regression (thick solid line). Contours show the density of matchup data points. Density of values has been normalized such that the maximum value is 1.0. Contours are drawn at 0.9, 0.8, 0.7, . . . , 0.1, 0.05.

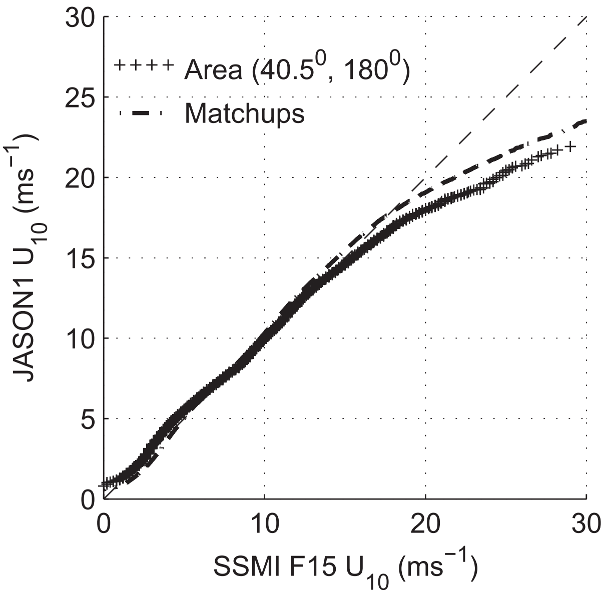

FIG. 10. Q–Q plot between *SSM/I F15* radiometer and *Jason-1* altimeter wind speeds. Case for matchup data between the two instruments (dashed–dotted line). Case where all data measured by both instruments within a 1° × 1° square centered on +45.5°, 180.5° are used (crosses). The fact that the data fall below the diagonal indicates that the altimeter underestimates wind speed at high values compared to the radiometer. Difference between the two lines is caused by spatial undersampling of extreme wind events by the altimeter.

the sampling patterns of the respective instruments influences the pdf. As noted earlier, the repeat cycle of the altimeter is such that it will retrace the same ground tracks only every 10 days for *Jason-1*. This means that it is possible that the altimeter misses some storms and hence ''undersamples'' extremes (Vinoth and Young 2011). Figure 10 confirms that the altimeter does undersample extreme conditions to some extent. The Q–Q plot for all data in a region shows that for the same probability level, *Jason-1* wind speeds are slightly lower than those for exact matchups. However, the undersampling does not appear to have a major impact. Note also that the analysis in Fig. 10 was repeated for a range of regions and produced very similar results to those shown in Fig. 10. Hence, it appears that both instruments have limitations when measuring high wind speeds. The altimeter transfer function ($U_{10} - \sigma_0$ relationship) appears to underestimate high wind speeds, whereas the radiometer fair weather bias also reduces the amount of high wind speed data in the tail of the pdf. The sparse ground track repeat frequency of the altimeter also misses some storms and hence slightly undersamples extreme conditions.

6. Error analysis

The buoy offset of -0.2 to $-0.35\,\mathrm{m\,s^{-1}}$ at $U_{10} = 7.5\,\mathrm{m\,s^{-1}}$ compared to the REMSS radiometer/scatterometer results and the cross-validation differences (altimeter to radiometer) of approximately $0.3\,\mathrm{m\,s^{-1}}$ raises the question of the cause of these differences. As a result, a number of sources of potential error were investigated. Issues that were investigated include 1) distance to shore of buoys used, 2) buoy–satellite matchup criteria, 3) sample size used for RMA analysis, 4) drag coefficient used to determine buoy U_{10}, and 5) confidence limits on RMA analysis. Finally, the high wind speed performance of the radiometer data is investigated using a limited number of measurements from a fixed offshore platform.

a. *Distance to shore of buoys*

The present analysis used only buoys more than 50 km offshore. This was intended to exclude satellite data that might be corrupted by the proximity to land. The chosen value (50 km) was based on the analysis of Zieger et al. (2009) for altimeter data. To test whether this value was responsible for the negative offset relative to the REMSS results for radiometer/scatterometer, the buoy matchup analysis was repeated with a range of different offshore values for the selection of buoys—50, 100, 150, 200, and 300 km. The analysis was carried out for SSM/I *F8*, SSM/I *F13*, and SSM/I *F17*. The resulting offsets at $U_{10} = 7.5\,\mathrm{m\,s^{-1}}$ were -0.381, -0.305, -0.478, -0.489, and $-0.341\,\mathrm{m\,s^{-1}}$ for SSM/I F08; -0.184, -0.256, -0.271, -0.262, and $-0.142\,\mathrm{m\,s^{-1}}$ for SSM/I *F13*; and -0.207, -0.142, -0.143, -0.128, and $-0.048\,\mathrm{m\,s^{-1}}$ for SSM/I *F17*, respectively. All values are negative, and there is no consistent trend that, for instance, may show the magnitude of the offset decreasing with distance offshore. The results do, however, show that the selection of buoys (i.e., as the offshore criterion changes, the actual buoys in the analysis change) can account for a difference of approximately $0.2\,\mathrm{m\,s^{-1}}$ in the offset. Hence, we conclude that using only buoys more than 50 km offshore does not bias the matchup analysis.

b. *Matchup criteria*

The matchup criteria used in the abovementioned analysis was $\Delta x = 50$ km and $\Delta t = 30$ min. These criteria were varied to see whether smaller values reduced the offset at $U_{10} = 7.5\,\mathrm{m\,s^{-1}}$. Values of $\Delta x = 50$ and 25 km and $\Delta t = 30$ and 15 min were investigated. The resulting offsets for $\Delta x = 50$ and 25 km were -0.381 and $-0.286\,\mathrm{m\,s^{-1}}$ for SSM/I *F8*, -0.184 and $-0.132\,\mathrm{m\,s^{-1}}$ for SSM/I F13, and -0.207 and $-0.255\,\mathrm{m\,s^{-1}}$ for SSM/I *F17*, respectively.

For $\Delta t = 30$ and 15 min, the offsets were -0.381 and $-0.390\,\mathrm{m\,s^{-1}}$ for SSM/I *F8*, -0.184 and $-0.033\,\mathrm{m\,s^{-1}}$ for SSM/I *F13*, and -0.207 and $-0.209\,\mathrm{m\,s^{-1}}$ for SSM/I *F17*, respectively. Again, there was no clear reduction in the offset as the matchup criteria were reduced. Therefore, we conclude that the matchup criteria used do not result in a negative offset.

c. Sample size

As noted above, the radiometer/scatterometer buoy matchups contain many collocation points. For instance, SSM/I *F13* has 163 377 points used in the RMA buoy analysis (Table A4). To determine whether the selection and number of points in the analysis had an impact on the result, the points were resampled. Initially, the matchup dataset was subsampled randomly in groups of 30 000 points. The RMA analysis for these subsampled groups gave almost identical regression results to the full analysis of Table A4. Across five different subsamples, the buoy offset at $U_{10} = 7.5\,\mathrm{m\,s^{-1}}$ varied by only $0.01\,\mathrm{m\,s^{-1}}$, indicating that these large data samples are little impacted by such subsampling.

In a second such analysis, the subsamples were selected across individual groups of buoys (i.e., not random); that is, 30 000 points were selected from one group of buoys and then a second 30 000 from a different group. The groups were not specifically selected on regional grounds, although this may also impact the results. Across six such selections of points, the offsets at $U_{10} = 7.5\,\mathrm{m\,s^{-1}}$ were -0.412, -0.224, -0.155, -0.143, -0.077, and $-0.127\,\mathrm{m\,s^{-1}}$. This analysis shows that the selection of buoys can account for differences in this offset of up to $0.25\,\mathrm{m\,s^{-1}}$. The exact cause of these differences is unknown, although it is most likely an indication of the accuracy of anemometer calibration across the buoys, possibly the effects of flow distortion around different buoys and boundary layer correction. Such differences do not account for the consistent small negative bias noted above, but they easily account for the differences between the calibration results noted for individual radiometer/scatterometer missions.

d. Drag coefficient

Buoy data are recorded at a variety of anemometer heights, although the significant majority of the data are from buoys where the anemometers are less than 5 m above the mean sea level. These data were converted to a reference height of 10 m using a value of the drag coefficient C_d and the assumption of a logarithmic boundary layer profile [(2)]. The impact of different values for C_d was assessed for the NDBC buoy results of SSM/I *F13*. The resulting buoy offsets at $U_{10} = 7.5\,\mathrm{m\,s^{-1}}$ were -0.184, -0.168, and $-0.059\,\mathrm{m\,s^{-1}}$ for $C_d = 1.2 \times 10^{-3}$, 1.3×10^{-3}, and 2.0×10^{-3}, respectively. A value of $C_d = 1.2 \times 10^{-3}$ was used in this analysis; $C_d = 1.3 \times 10^{-3}$ was used in the earlier REMSS analysis of Mears et al. (2001). The offset reduces as the value of C_d increases, and a value of $C_d = 2.0 \times 10^{-3}$ almost completely removes the offset. It is not clear what value of C_d has been used by REMSS in the development of SSMI algorithm, version 7, in Wentz (2013). A sea state–dependent value of C_d was also tested (Donelan 1982), yielding an offset of $-0.166\,\mathrm{m\,s^{-1}}$, which is in reasonable agreement with the value $C_d = 1.2 \times 10^{-3}$ used in the present analysis. As noted above, measured values of C_d can scatter over an order of magnitude. Therefore, the observed offset between REMSS values and the present buoy results could be the result of different assumed values of the drag coefficient.

e. Confidence limits

The data cloud in Fig. 6 is indicative of the fact that there are sampling and measurements errors in both the buoy measurements of wind speed and the radiometer measurements. The RMA regression analysis and the confidence limits calculated using the approach of Ricker (1973) should account for the variability of such data. Because of the large number of data points in the analysis, the confidence limits on the regression are very small (see Table A4). An alternative Monte Carlo approach to estimating the confidence limits was investigated. The data cloud in Fig. 6a (SSM/I *F13*) can be approximated by a two-dimensional Gaussian distribution with $\sigma = 0.87\,\mathrm{m\,s^{-1}}$ in both dimensions of the buoy wind speed and the radiometer wind speed. Each of the 163 377 points in the buoy–SSM/I *F13* matchup analysis was considered to be a random Gaussian variable with a mean given by the measured value and $\sigma = 0.87\,\mathrm{m\,s^{-1}}$. A total of 1000 realizations of each of these points following this probability distribution were generated and the RMA analysis was conducted for each of the realizations. The slope and intercept of each of the 1000 realizations were rank ordered and the 5% and 95% values determined. The resulting confidence limits for SSM/I *F13* are slope $m = 0.987 \pm 0.002$ and intercept $c = -0.086 \pm 0.012$, with the offset at $U_{10} = 7.5\,\mathrm{m\,s^{-1}}$, $\Delta U_{10} = -0.183 \pm 0.005\,\mathrm{m\,s^{-1}}$. These error values are extremely close to the Ricker (1973) results in Table A4 and confirm that the confidence limits for these random errors are extremely small due to the very large datasets. As noted above, however, systematic errors such as those brought about

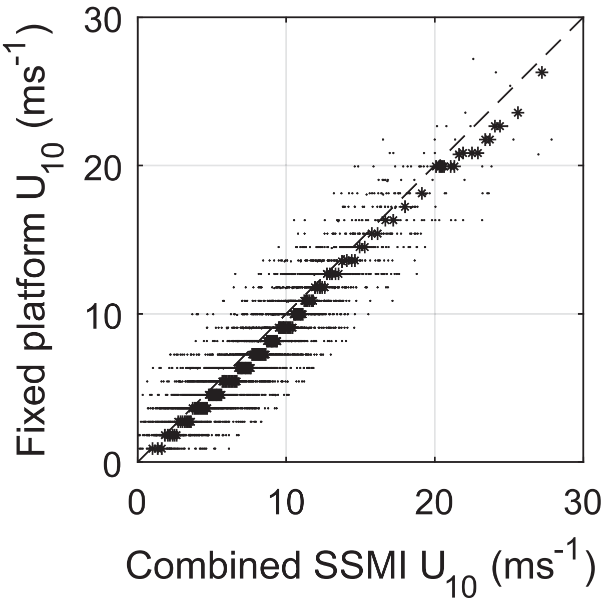

FIG. 11. Comparison of combined SSM/I wind speeds from *F8–F17* with wind speeds measured at a fixed platform at +61.6°, +3.7° (small dots). The small-dot data points fall into horizontal lines as the data are archived in increments of 1 m s^{-1}. Q–Q plot for these data is shown by the asterisk (*).

through anemometer calibration are potentially significantly larger.

f. High wind calibration

The Q–Q analysis in section 4 indicated that for wind speeds above 15 m s^{-1}, the altimeter and buoys are in good agreement, whereas the radiometers/scatterometer measures higher values than the buoys. As a number of studies indicate that buoys underestimate at high winds, the radiometer/scatterometer result is in the appropriate direction; however, whether the magnitude of the increase above buoy measurements is correct requires further data. The problem, however, is that there is little reliable high wind ground truth (not buoy) data. Within the ECMWF composite wind dataset, one location at +61.6°, 3.7° is a fixed North Sea oil platform with an anemometer height of 33 m. Although oil platforms are not ideal for the measurement of wind speed, because of flow disturbance around the structure, this location provides the opportunity to investigate the radiometer Q–Q performance at high wind speed for a fixed measurement platform.

As the amount of data at this single location for any one radiometer is relatively small, data were pooled from all SSM/I missions (*F10–F17*). In this manner, a total of 5400 matchups were obtained. Figure 11 shows the (platform–radiometer) matchup points and the Q–Q plot. The RMA regression result for the combined data is $U_{10}^{*} = 0.976U_{10} - 0.135$, with an offset at $U_{10} = 7.5$ m s^{-1} of -0.32 m s^{-1}. Both the regression result and the offset are in remarkably good agreement with the buoy results in Table A4. As the anemometer values needed to be corrected from a height of 33 m, this good agreement suggests that the drag coefficient used in this analysis is reasonable. More importantly, the Q–Q plot indicates that the pdfs of the platform U_{10} and the radiometer are in reasonable agreement. In contrast to the buoy matchup data (Fig. 8a), the platform wind speeds are in good agreement with the radiometers at high wind speeds. Although data from a single location is not definitive, this result suggests that the REMSS radiometer results perform reasonably well above $U_{10} = 15$ m s^{-1}, whereas the altimeter underestimates such high wind speeds.

7. Conclusions

This paper presents the calibration and validation of a combined satellite database consisting of nine altimeters, 12 radiometers, and two scatterometers that have flown over the last 30 years. All instruments are calibrated in a consistent manner against the NDBC buoy dataset and then validated against an independent buoy dataset. The various satellite missions are cross validated at matchup points, where they overfly the same region of the ocean at approximately the same time. The calibrated satellite datasets were checked for consistency as a function of time. Where instrument drift or discontinuities were detected, these were corrected and documented.

The altimeter calibrations are consistent with those previously undertaken by Ash et al. (2010) for Globwave data. In particular, periods of instrumental drift for TOPEX H_s and *GFO* U_{10} are identified and functions to correct such drift are proposed. As identified by Zieger et al. (2009), a number of discontinuities in the altimeter records are identified. In the case of *ERS-1* and *ERS-2*, U_{10} corrections are large, 20% for *ERS-1* and 10% for *ERS-2* (Table A1). Again, this is consistent with Ash et al. (2010). These issues demonstrate the importance of such calibrations before using altimeter data.

In contrast to the altimeter data, the REMSS radiometer/scatterometer data are a high-quality and consistent U_{10} dataset. Comparisons with buoys indicate a small negative bias (buoys less than radiometer/scatterometer) of approximate 3%. At a mean global wind speed of 7.5 m s^{-1}, this offset represents a reduction in REMSS values of between -0.2 and -0.3 m s^{-1}. An extensive error analysis is undertaken to attempt

TABLE A1. RMA altimeter calibration relations for the full missions using the NDBC buoy dataset. Slope and offset of the RMA regression are listed with 95% confidence values for both of these quantities. Number of matchup data points in the regression (n) and percentage of outliers excluded from the RMA regression are listed.

	Altimeter	Slope	Offset	95% limit slope	95% limit offset	n	Outlier (%)
H_s	*Geosat*	0.961	0.053	0.924 to 0.997	−0.035 to 0.141	467	5.4
	ERS-1	1.213	−0.056	1.184 to 1.242	−0.121 to 0.009	1578	5.7
	TOPEX	1.061	−0.094	1.053 to 1.070	−0.110 to −0.078	8416	5.9
	ERS-2	1.110	−0.090	1.096 to 1.123	−0.117 to −0.062	5658	6.3
	GFO	1.069	0.089	1.058 to 1.080	0.068 to 0.110	4533	8.3
	Jason-1	1.060	−0.078	1.051 to 1.069	−0.096 to −0.060	7732	6.9
	Envisat	1.007	0.044	0.998 to 1.016	0.026 to 0.062	7584	7.2
	Jason-2	1.061	−0.099	1.049 to 1.073	−0.123 to −0.074	4627	8.1
	CryoSat	1.001	−0.123	0.985 to 1.017	−0.157 to −0.090	2862	5.7
U_{10}	*Geosat*	1.065	−0.880	1.001 to 1.128	−1.356 to −0.405	575	0.7
	ERS-1	1.017	−0.543	0.0990 to 1.044	−0.751 to −0.335	2625	1.6
	TOPEX	0.999	−0.420	0.985 to 1.014	−0.533 to −0.307	8618	1.6
	ERS-2	0.975	−0.182	0.961 to 0.989	−0.287 to −0.077	9647	1.4
	GFO	1.039	−0.563	1.017 to 1.062	−0.742 to −0.383	4593	1.1
	Jason-1	0.976	−0.258	0.963 to 0.990	−0.360 to −0.157	9081	1.9
	Envisat	1.030	−0.617	1.016 to 1.044	−0.726 to −0.509	9972	2.0
	Jason-2	0.971	−0.253	0.955 to 0.987	−0.372 to −0.135	6868	1.9
	CryoSat	0.985	−0.400	0.964 to 1.006	−0.556 to −0.242	3934	1.3

to identify the basis of this difference. It is determined that different assumed values of the drag coefficient used to adjust buoy wind speeds to a reference height of 10 m could account for an offset of this magnitude. Also, differences of this magnitude can occur if different groups of buoys are used in the matchup analysis. This indicates that calibration differences between different sets of buoys are of order $0.3\,\mathrm{m\,s^{-1}}$. Hence, although the present analysis indicates a negative offset in the REMSS radiometer/scatterometer calibration, it is of the same order as the accuracy of the buoy wind speed measurements.

The performance of the satellite systems was also investigated across the full magnitude of the measured values of U_{10} and H_s. This analysis shows that the altimeter provides values of H_s consistent with buoy

TABLE A2. RMA altimeter calibration relations for the full missions using the ECMWF composite buoy dataset. Slope and offset of the RMA regression are listed with 95% confidence values for both these quantities. Number of matchup data points in the regression n and percentage of outliers excluded from the RMA regression are listed.

	Altimeter	Slope	Offset	95% limit slope	95% limit offset	n	Outlier (%)
H_s	*Geosat*						
	ERS-1	1.098	0.169	1.051 to 1.145	0.047 to 0.290	831	2.8
	TOPEX	0.980	−0.046	0.972 to 0.988	−0.066 to −0.027	12 719	4.2
	ERS-2	1.050	−0.070	1.039 to 1.060	−0.097 to −0.043	10 127	4.1
	GFO	1.000	0.091	0.989 to 1.011	0.065 to 0.116	6257	5.6
	Jason-1	1.010	−0.108	1.002 to 1.017	−0.127 to −0.088	14 322	4.5
	Envisat	0.990	−0.039	0.981 to 0.999	−0.062 to −0.015	9827	5.8
	Jason-2	1.023	−0.148	1.013 to 1.033	−0.174 to −0.122	8691	4.5
	CryoSat	1.004	−0.222	0.990 to 1.019	−0.262 to −0.181	2568	6.5
U_{10}	*Geosat*						
	ERS-1	1.018	−0.403	0.978 to 1.058	−0.761 to −0.046	1279	1.3
	TOPEX	1.001	−0.739	0.989 to 1.013	−0.845 to −0.632	15 014	0.8
	ERS-2	0.942	−0.420	0.930 to 0.955	−0.533 to −0.307	12 584	0.5
	GFO	1.014	−0.631	0.996 to 1.031	−0.775 to −0.486	8154	0.7
	Jason-1	0.940	−0.388	0.931 to 0.949	−0.468 to −0.308	20 292	1.0
	Envisat	0.965	−0.569	0.953 to 0.978	−0.676 to −0.461	12 322	0.9
	Jason-2	0.935	−0.402	0.924 to 0.947	−0.499 to −0.305	13 610	1.1
	CryoSat	0.959	−0.374	0.942 to 0.976	−0.508 to −0.239	5364	1.8

TABLE A3. RMA altimeter calibration relations as in Table A1, but using piecewise regressions to account for discontinuities in the calibrations as a function of time. Drift removal functions are also stated where appropriate.

	Altimeter	Period	Calibration relation	95% limit slope	95% limit offset	n	Outlier (%)
H_s	*Geosat*	31 Mar 1985–30 Dec 1989	$H_s^* = 0.961H_s + 0.053$	0.924 to 0.997	−0.035 to 0.141	467	5.4
	ERS-1	1 Aug 1991–2 Jun 1996	$H_s^* = 1.213H_s - 0.056$	1.184 to 1.242	−0.121 to 0.009	1578	5.7
	TOPEX	25 Sep 1992–25 Apr 1997	$H_s^* = 1.051H_s - 0.060$	1.035 to 1.068	−0.090 to −0.030	2402	5.9
	TOPEX	25 Apr 1997–30 Jan 1999	$H_s^* = H_s + 0.0303 - 0.0542[\exp(0.0027t)]^{1.1080}$	—	—	—	—
	TOPEX	30 Jan 1999–8 Oct 2005	$H_s^* = 1.065H_s - 0.080$	1.055 to 1.075	−0.099 to −0.060	5110	6.8
	ERS-2	29 Apr 1995–11 May 2009	$H_s^* = 1.110H_s - 0.090$	1.096 to 1.123	−0.117 to −0.062	5658	6.3
	GFO	7 Jan 2000–7 Sep 2008	$H_s^* = 1.069H_s + 0.089$	1.058 to 1.080	0.068 to 0.110	4533	8.3
	Jason-1	15 Jan 2002–3 Mar 2012	$H_s^* = 1.060H_s - 0.078$	1.051 to 1.069	−0.096 to −0.060	7732	6.9
	Envisat	14 May 2002–1 Aug 2004	$H_s^* = 1.033H_s + 0.004$	1.009 to 1.058	−0.045 to −0.052	1078	7.5
	Envisat	1 Aug 2004–8 Apr 2012	$H_s^* = 1.003H_s + 0.052$	0.994 to 1.013	0.032 to 0.071	6506	7.2
	Jason-2	22 Jun 2008–10 May 2012	$H_s^* = 1.061H_s - 0.099$	1.049 to 1.073	−0.123 to −0.074	4627	8.1
	CryoSat	14 Jul 2010–1 Apr 2015	$H_s^* = 1.001H_s - 0.123$	0.985 to 1.017	−0.157 to −0.090	2862	5.7
U_{16}	*Geosat*	31 Mar 1985–30 Dec 1989	$U_{10}^* = 1.065U_{10} - 0.880$	1.001 to 1.128	−1.356 to −0.405	575	0.7
	ERS-1	1 Aug 1991–2 Jun 1996	$U_{10}^* = 1.017U_{10} - 0.543$	0.0990 to 1.044	−0.751 to −0.335	2625	1.6
	TOPEX	25 Sep 1992–8 Oct 2005	$U_{10}^* = 0.999U_{10} - 0.420$	0.985 to 1.014	−0.533 to −0.307	8618	1.6
	ERS-2	29 Apr 1995–1 Jan 2000	$U_{10}^* = 0.979U_{10} + 0.032$	0.953 to 1.005	−0.157 to −0.222	2918	1.4
	ERS-2	1 Jan 2000–1 Jan 2001	$U_{10}^* = 1.002U_{10} - 0.565$	0.949 to 1.056	−0.985 to −0.145	650	1.5
	ERS-2	1 Jan 2001–1 Apr 2001	$U_{10}^* = 0.952U_{10} - 1.389$	0.801 to 1.103	−2.905 to 0.127	126	0.8
	ERS-2	1 Apr 2001–1 Jun 2005	$U_{10}^* = 0.953U_{10} - 0.294$	0.928 to 0.978	−0.490 to −0.098	2878	1.6
	ERS-2	1 Jun 2005–11 May 2009	$U_{10}^* = 1.017U_{10} - 0.350$	0.992 to 1.043	−0.532 to −0.168	3075	1.2
	GFO	7 Jan 2000–1 Jan 2001	$U_{10}^* = 0.972U_{10} - 0.477$	0.869 to 1.075	−1.556 to −0.202	200	2.0
	GFO	1 Jan 2001–1 Mar 2006	$U_{10}^* = 1.085U_{10} - 0.240$	1.057 to 1.112	−0.649 to −0.230	2900	2.5
	GFO	1 Mar 2006–7 Sep 2008	$U_{10}^* = U_{10} - 0.0025t + 0.2$	—	—	—	—
	Jason-1	15 Jan 2002–3 Mar 2012	$U_{10}^* = 0.976U_{10} - 0.258$	0.963 to 0.990	−0.360 to −0.157	9081	1.9
	Envisat	14 May 2002–8 Apr 2012	$U_{10}^* = 1.030U_{10} - 0.617$	1.016 to 1.044	−0.726 to −0.509	9972	2.0
	Jason-2	22 Jun 2008–10 May 2012	$U_{10}^* = 0.971U_{10} - 0.253$	0.955 to 0.987	−0.372 to −0.135	6868	1.9
	CryoSat	14 Jul 2010–1 Feb 2011	$U_{10}^* = 0.978U_{10} - 0.854$	0.930 to 1.026	−1.221 to −0.487	710	1.1
	CryoSat	1 Feb 2011–1 Apr 2015	$U_{10}^* = 0.983U_{10} - 0.270$	0.960 to 1.007	−0.442 to −0.098	3224	1.6

data across the full range of available data (0–10 m). Across the range 0–15 m s^{-1}, altimeter, radiometer, and scatterometer instruments also provide values of U_{10} that are consistent with buoy data and between the various instrument systems. For wind speeds above 15 m s^{-1}, the altimeter appears to underestimate U_{10}, whereas the radiometer/scatterometer data appear in reasonable agreement with the limited fixed-platform anemometer data. Buoy data tend to underestimate wind speeds at high values of wind speed. The

TABLE A4. RMA radiometer and scatterometer calibration relations for the full missions using the NDBC buoy dataset. Slope and offset of the RMA regression are listed with 95% confidence values for both these quantities. Number of matchup data points in the regression n and the percentage of outliers excluded from the RMA regression are listed. The asterisk denotes values corrected by the calibration.

	Satellite	Sensor	Calibration relation	95% limit slope	95% limit offset	n	Out (%)
U_{10}	SSM/I *F8*	Radiometer	$U_{10}^* = 0.961U_{10} - 0.088$	0.956 to 0.966	−0.126 to −0.050	24 711	0.4
	SSM/I *F10*	Radiometer	$U_{10}^* = 0.966U_{10} - 0.133$	0.963 to 0.970	−0.161 to −0.105	40 864	0.7
	SSM/I *F11*	Radiometer	$U_{10}^* = 0.971U_{10} - 0.138$	0.968 to 0.975	−0.162 to −0.114	55 903	0.8
	SSM/I *F13*	Radiometer	$U_{10}^* = 0.987U_{10} - 0.086$	0.986 to 0.989	−0.100 to −0.072	163 377	0.7
	SSM/I *F14*	Radiometer	$U_{10}^* = 0.984U_{10} + 0.007$	0.982 to 0.987	−0.008 to 0.023	117 691	0.8
	SSM/I *F15*	Radiometer	$U_{10}^* = 0.984U_{10} - 0.032$	0.982 to 0.986	−0.045 to −0.018	166 287	0.9
	SSM/I *F16*	Radiometer	$U_{10}^* = 0.977U_{10} - 0.060$	0.975 to 0.979	−0.072 to −0.047	191 116	1.0
	SSM/I *F17*	Radiometer	$U_{10}^* = 0.975U_{10} - 0.019$	0.973 to 0.976	−0.034 to −0.005	137 167	1.1
	AMSR-E–LF	Radiometer	$U_{10}^* = 1.009U_{10} - 0.228$	1.007 to 1.011	−0.241 to −0.216	15 0386	1.0
	AMSR-E–MF	Radiometer	$U_{10}^* = 0.990U_{10} - 0.013$	0.988 to 0.992	−0.025 to 0.000	151 186	1.0
	TMI–LF	Radiometer	$U_{10}^* = 0.981U_{10} - 0.160$	0.979 to 0.983	−0.171 to −0.145	183 316	1.1
	TMI–MF	Radiometer	$U_{10}^* = 0.959U_{10} + 0.189$	0.957 to 0.962	0.173 to 0.205	116 228	0.5
	WindSat	Radiometer	$U_{10}^* = 1.005U_{10} - 0.282$	1.003 to 1.007	−0.296 to −0.267	124 599	1.3
	QuikSCAT	Scatterometer	$U_{10}^* = 1.010U_{10} - 0.235$	1.008 to 1.011	−0.247 to −0.223	161 203	1.6

TABLE A5. RMA radiometer and scatterometer calibration relations for the full missions using the ECMWF composite buoy dataset. Slope and offset of the RMA regression are listed with 95% confidence values for both these quantities. Number of matchup data points in the regression (n) and the percentage of outliers excluded from the RMA regression are listed. The asterisk denotes values corrected by the calibration.

	Satellite	Sensor	Calibration relation	95% limit slope	95% limit offset	n	Out (%)
U_{10}	SSM/I *F8*	Radiometer					
	SSM/I *F10*	Radiometer	$U_{10}^* = 0.977U_{10} - 0.087$	0.973–0.982	−0.129 to −0.046	29 966	0.4
	SSM/I *F11*	Radiometer	$U_{10}^* = 0.951U_{10} + 0.055$	0.948–0.955	0.029 to 0.082	65 158	0.8
	SSM/I *F13*	Radiometer	$U_{10}^* = 0.958U_{10} - 0.044$	0.956–0.959	−0.056 to −0.032	268 086	0.8
	SSM/I *F14*	Radiometer	$U_{10}^* = 0.947U_{10} - 0.002$	0.945–0.948	−0.016 to 0.013	203 960	0.7
	SSM/I *F15*	Radiometer	$U_{10}^* = 0.954U_{10} - 0.106$	0.953–0.996	−0.118 to −0.093	276 762	0.8
	SSM/I *F16*	Radiometer	$U_{10}^* = 0.950U_{10} - 0.012$	0.949–0.952	−0.023 to −0.001	341 594	0.1
	SSM/I *F17*	Radiometer	$U_{10}^* = 0.955U_{10} - 0.016$	0.953–0.956	−0.029 to −0.003	224 169	1.0
	AMSR-E–LF	Radiometer	$U_{10}^* = 0.966U_{10} - 0.041$	0.965–0.967	−0.051 to −0.030	284 806	1.0
	AMSR-E–MF	Radiometer	$U_{10}^* = 0.955U_{10} + 0.055$	0.953–0.956	0.045 to 0.065	325 612	1.0
	TMI–LF	Radiometer	$U_{10}^* = 0.988U_{10} - 0.022$	0.985–0.990	−0.039 to −0.005	114 532	0.9
	TMI–MF	Radiometer	$U_{10}^* = 0.959U_{10} + 0.189$	0.957–0.962	0.173 to 0.205	116 228	0.5
	WindSat	Radiometer	$U_{10}^* = 0.975U_{10} - 0.257$	0.974–0.977	−0.270 to −0.244	223 210	1.1
	QuikSCAT	Scatterometer	$U_{10}^* = 0.984U_{10} - 0.253$	0.983–0.986	−0.264 to −0.241	277 560	1.2

radiometer and scatterometer cannot accurately measure wind speed in heavy rain. The exclusion of these cases, which often are associated with high winds, produces a fair weather bias. The distance between altimeter tracks is often many hundreds of kilometers and the repeat time for a given track up to 10 days. This relatively course spatial coverage means that the altimeter potentially undersamples storm events and may miss wind speed extremes. Cross validation between the instruments confirms that the altimeter underestimates extreme wind speeds.

As reliable ground truth calibration data at high wind speeds are very limited, all systems (altimeter, radiometer, scatterometer) should be used with caution for wind speeds greater than $20\,\mathrm{m\,s^{-1}}$.

The final calibrated combined satellite database provides a valuable resource for the study of a wide range of ocean issues, including engineering design, ship routing, air–sea interaction, climatology, climate change, and model validation. Both of the datasets used in this study are available in the public domain (altimeter—Globwave, http://globwave.ifremer.fr/; radiometer/scatterometer—Remote Sensing Systems (REMSS), http://www.remss.com/). The matchup data are available from the corresponding author by request.

Acknowledgments. This work was financially supported by the Australian Research Council (ARC) through Discovery Grant DP130100215 and the U.S. Office of Naval Research (ONR) through Grant N00014-13-1-0278. This support has been invaluable in completing this extensive study. The raw datasets used in the study were supplied by Globwave (altimeter and buoy) and Remote Sensing Systems (RSS) (radiometer/scatterometer). Without these public domain archives the study would have been extremely difficult.

APPENDIX

Calibration and Validation Relationships

The tables in the appendix show relationships for missions using various datasets. See Tables A1, A2, A3, A4, and A5.

REFERENCES

Abdalla, S., 2007: Ku-band radar altimeter surface wind speed algorithm. *Proceedings of the Envisat Symposium 2007*, H. Lacoste and L. Ouwehand, Eds., ESA SP-636, 463250. [Available online at https://earth.esa.int/workshops/envisatsymposium/proceedings/sessions/3E4/463250sa.pdf.]

Alpers, W. R., D. B. Ross, and C. L. Rufenach, 1981: On the detectability of ocean surface waves by real and synthetic aperture radar. *J. Geophys. Res.*, **86**, 6481–6498, doi:10.1029/JC086iC07p06481.

Alves, J. H. G. M., and I. R. Young, 2003: On estimating extreme wave heights using combined Geosat, Topex/Poseidon and ERS-1 altimeter data. *Appl. Ocean Res.*, **25**, 167–186, doi:10.1016/j.apor.2004.01.002.

Ash, E., D. Carter, and F. Collard, 2010: Globwave satellite wave data quality report. D.16, Version 1.2, Logica UK Ltd., 69 pp. [Available online at http://globwave.ifremer.fr/download/GlobWave_D.16_SWDQR.pdf.]

Atlas, R., R. N. Hoffman, J. Ardizzone, S. M. Leidner, J. C. Jusem, D. K. Smith, and D. Gombos, 2011: A cross-calibrated, multiplatform ocean surface wind velocity product for meteorological and oceanographic applications. *Bull. Amer. Meteor. Soc.*, **92**, 157–174, doi:10.1175/2010BAMS2946.1.

Bendat, J. S., and A. G. Piersol, 1971: *Random Data: Analysis and Measurement Procedures*. Wiley-Interscience, 407 pp.

Bender, L. C., N. L. Guinasso, and J. N. Walpert, 2010: A comparison of methods for determining significant wave heights—Applied to a 3-m discus buoy during Hurricane Katrina. *J. Atmos. Oceanic Technol.*, **27**, 1012–1028, doi:10.1175/2010JTECHO724.1.

Callahan, P. S., C. S. Morris, and S. V. Hsiao, 1994: Comparison of TOPEX/POSEIDON σ_0 and significant wave height distributions to Geosat. *J. Geophys. Res.*, **99**, 25 015–25 024, doi:10.1029/94JC01759.

Chelton, D. B., J. C. Ries, B. J. Haines, L.-L. Fu, and P. S. Callahan, 2001: Satellite altimetry. *Satellite Altimetry and Earth Sciences: A Handbook of Techniques and Applications*, L.-L. Fu and A. Cazenave, Eds., International Geophysics Series, Vol. 69, Academic Press, 1–131.

Cheney, R. E., B. C. Douglas, R. W. Agreen, L. Miller, D. L. Porter, and N. Doyle, 1987: GEOSAT altimeter geophysical data record: User handbook. NOAA Tech. Memo. NOS-NGS-46, 32 pp.

Cotton, P. D., and D. J. T. Carter, 1994: Cross calibration of TOPEX, ERS-1, and Geosat wave heights. *J. Geophys. Res.*, **99**, 25 025–25 033, doi:10.1029/94JC02131.

Dobson, E., F. Monaldo, J. Goldhirsh, and J. Wilkerson, 1987: Validation of Geosat altimeter-derived wind speeds and significant wave heights using buoy data. *J. Geophys. Res.*, **92**, 10 719–10 731, doi:10.1029/JC092iC10p10719.

Donelan, M. A., 1982: The dependence of the aerodynamic drag coefficient on wave parameters. *Proc. First Int. Conf. on the Meteorology and Air–Sea Interaction of the Coastal Zone*, The Hague, Netherlands, Amer. Meteor. Soc., 381–387.

Dorandeu, J., 1999: Side-B TOPEX altimeter evaluation. CLS/DOS/NT Rep. 99.175, 124 pp.

Durrant, T. H., D. J. M. Greenslade, and I. Simmonds, 2009: Validation of *Jason-1* and *Envisat* remotely sensed wave heights. *J. Atmos. Oceanic Technol.*, **26**, 123–134, doi:10.1175/2008JTECHO598.1.

Evans, D., C. L. Conrad, and F. M. Paul, 2003: Handbook of automated data quality control checks and procedures of the National Data Buoy Center. NOAA/National Data Buoy Center Tech. Doc. 03-02, 44 pp.

Gemmrich, J., B. Thomas, and R. Bouchard, 2011: Observational changes and trends in northeast Pacific wave records. *Geophys. Res. Lett.*, **38**, L22601, doi:10.1029/2011GL049518.

Gower, J. F. R., 1996: Intercalibration of wave and wind data from TOPEX/POSEIDON and moored buoys off the west coast of Canada. *J. Geophys. Res.*, **101**, 3817–3829, doi:10.1029/95JC03281.

Guan, C., and L. Xie, 2004: On the linear parameterization of drag coefficient over sea surface. *J. Phys. Oceanogr.*, **34**, 2847–2851, doi:10.1175/JPO2664.1.

Hasselmann, K., and S. Hasselmann, 1991: On the nonlinear mapping of an ocean wave spectrum into a synthetic aperture radar image spectrum and its inversion. *J. Geophys. Res.*, **96**, 10 713–10 729, doi:10.1029/91JC00302.

——, R. K. Raney, W. J. Plant, W. Alpers, R. A. Shuchman, D. R. Lyzenga, C. L. Rufenach, and M. J. Tucker, 1985: Theory of synthetic aperture radar ocean imaging: A MARSEN view. *J. Geophys. Res.*, **90**, 4659–4686, doi:10.1029/JC090iC03p04659.

Henderson, F. M., and A. J. Lewis, Eds., 1998: *Principles and Applications of Imaging Radar*. Vol. 2, *Manual of Remote Sensing*, 3rd ed. John Wiley & Sons, Inc., 896 pp.

Hoffman, R. N., J. V. Ardizzone, S. M. Leidner, D. K. Smith, and R. Atlas, 2013: Error estimates for ocean surface winds: Applying Desroziers diagnostics to the cross-calibrated, multiplatform analysis of wind speed. *J. Atmos. Oceanic Technol.*, **30**, 2596–2603, doi:10.1175/JTECH-D-13-00018.1.

Holland, P. W., and R. E. Welsch, 1977: Robust regression using iterative reweighted least-squares. *Comm. Stat. Theory Methods*, **6**, 813–827, doi:10.1080/03610927708827533.

Hollinger, J., J. L. Pierce, and G. Poe, 1990: SSM/I instrument evaluation. *IEEE Trans. Geosci. Remote Sens.*, **28**, 781–790, doi:10.1109/36.58964.

Holthuijsen, L. H., 2007: *Waves in Oceanic and Coastal Waters*. Cambridge University Press, 387 pp.

Howden, S., D. Gilhousen, N. Guinasso, J. Walpert, M. Sturgeon, and L. Bender, 2008: Hurricane Katrina winds measured by a buoy-mounted sonic anemometer. *J. Atmos. Oceanic Technol.*, **25**, 607–616.

Jensen, R. E., V. R. Swail, R. H. Bouchard, R. E. Riley, T. J. Hesser, M. Blaseckie, and C. MacIsaac, 2015: Field Laboratory for Ocean Sea State Investigation and Experimentation: FLOSSIE: Intra-measurement evaluation of 6N wave buoy systems. *14th Int. Workshop on Wave Hindcasting and Forecasting and Fifth Coastal Hazard Symposium*, Key West, FL, WMO/IOC JCOMM, A1. [Available online at http://www.waveworkshop.org/14thWaves/Papers/WW14%20FLOSSIE%20Jensen%20et%20al.pdf.]

Kramer, H. J., 1994: *Observation of the Earth and Its Environment: Survey of Missions and Sensors*. 2nd ed. Springer-Verlag, 580 pp.

Large, W. G., and S. Pond, 1982: Sensible and latent heat flux measurements over the ocean. *J. Phys. Oceanogr.*, **12**, 464–482, doi:10.1175/1520-0485(1982)012<0464:SALHFM>2.0.CO;2.

——, J. Morzel, and G. B. Crawford, 1995: Accounting for surface wave distortion of the marine wind profile in low-level ocean storms wind measurements. *J. Phys. Oceanogr.*, **25**, 2959–2971, doi:10.1175/1520-0485(1995)025<2959:AFSWDO>2.0.CO;2.

Li, X.-M., S. Lehner, and T. Bruns, 2011: Ocean wave integral parameter measurements using Envisat ASAR wave mode data. *IEEE Trans. Geosci. Remote Sens.*, **49**, 155–174, doi:10.1109/TGRS.2010.2052364.

Long, D. G., and M. R. Drinkwater, 1999: Cryosphere applications of NSCAT data. *IEEE Trans. Geosci. Remote Sens.*, **37**, 1671–1684, doi:10.1109/36.763287.

Mears, C. A., D. K. Smith, and F. J. Wentz, 2001: Comparison of Special Sensor Microwave Imager and buoy-measured wind speeds from 1987 to 1997. *J. Geophys. Res.*, **106**, 11 719–11 729, doi:10.1029/1999JC000097.

Meissner, T., and F. J. Wentz, 2009: Wind vector retrievals under rain with passive satellite microwave radiometers. *IEEE Trans. Geosci. Remote Sens.*, **47**, 3065–3083, doi:10.1109/TGRS.2009.2027012.

——, and ——, 2012: The emissivity of the ocean surface between 6 and 90 GHz over a large range of wind speeds and Earth incidence angles. *IEEE Trans. Geosci. Remote Sens.*, **50**, 3004–3026, doi:10.1109/TGRS.2011.2179662.

Monaldo, F., 1988: Expected differences between buoy and radar altimeter estimates of wind speed and significant wave height and their implications on buoy-altimeter comparisons. *J. Geophys. Res.*, **93**, 2285–2302, doi:10.1029/JC093iC03p02285.

Naderi, F., M. H. Freilich, and D. G. Long, 1991: Spaceborne radar measurement of wind velocity over the ocean—An overview of the NSCAT scatterometer system. *Proc. IEEE*, **79**, 850–866, doi:10.1109/5.90163.

Qi, C., and Z. Zhao, 2015: Electromagnetic scattering and statistical analysis of clutter from oil contaminated sea surface. *Radioengineering*, **24**, 87–92.

Queffeulou, P., 2003: Validation of ENVISAT RA-2 and JASON-1 altimeter wind and wave measurements. *2003 IEEE International Geoscience and Remote Sensing Symposium; Learning from Earth's Shapes and Colors*, Vol. 5, IEEE, 2987–2989, doi:10.1109/IGARSS.2003.1294656.

——, 2004: Long-term validation of wave height measurements from altimeters. *Mar. Geod.*, **27**, 495–510, doi:10.1080/01490410490883478.

——, A. Bentamy, and J. Guyader, 2004: Satellite wave height validation over the Mediterranean Sea. *Proceedings of the 2004 Envisat and ERS Symposium*, H. Lacoste and L. Ouwehand, Eds., ESA SP-572, 333.

Rapizo, H., A. V. Babanin, E. Schulz, M. A. Hemer, and T. H. Durrant, 2015: Observation of wind-waves from a moored buoy in the Southern Ocean. *Ocean Dyn.*, **65**, 1275–1288, doi:10.1007/s10236-015-0873-3.

Ricker, W. E., 1973: Linear regression in fishery research. *J. Fish. Res. Board Can.*, **30**, 409–434, doi:10.1139/f73-072.

Spencer, M. W., C. Wu, and D. G. Long, 2000: Improved resolution backscatter measurements with the SeaWinds pencil-beam scatterometer. *IEEE Trans. Geosci. Remote Sens.*, **38**, 89–104, doi:10.1109/36.823904.

Stoffelen, A., 1998: Toward the true near-surface wind speed: Error modeling and calibration using triple collocation. *J. Geophys. Res.*, **103**, 7755–7766, doi:10.1029/97JC03180.

Taylor, P. K., and M. J. Yelland, 2001: Comments on "On the effect of ocean waves on the kinetic energy balance and consequences for the inertial dissipation technique." *J. Phys. Oceanogr.*, **31**, 2532–2536, doi:10.1175/1520-0485(2001)031<2532:COOTEO>2.0.CO;2.

Trauth, M. H., 2007: *MATLAB Recipes for Earth Sciences*. 2nd ed. Springer Verlag, 288 pp.

Vinoth, J. and I. R. Young, 2011: Global estimates of extreme wind speed and wave height. *J. Climate*, **24**, 1647–1665, doi:10.1175/2010JCLI3680.1.

Walker, D. M., 1995: Measurement techniques and capabilities of the Geosat Follow-On (GFO) radar altimeter. *Proceedings of IEEE Second Topical Symposium on Combined Optical-Microwave Earth and Atmosphere Sensing*, IEEE, 226–228, doi:10.1109/COMEAS.1995.472314.

Wentz, F. J., 1997: A well-calibrated ocean algorithm for special sensor microwave/imager. *J. Geophys. Res.*, **102**, 8703–8718, doi:10.1029/96JC01751.

——, 2013: SSM/I version-7 calibration report. RSS Tech. Rep. 011012, 44 pp. [Available online at http://images.remss.com/papers/rsstech/2012_011012_Wentz_Version-7_SSMI_Calibration.pdf.]

Young, I. R., 1986: Probability distribution of spectral integrals. *J. Waterw., Port Coastal Ocean Eng.*, **112**, 338–341, doi:10.1061/(ASCE)0733-950X(1986)112:2(338).

——, 1993: An estimate of the Geosat altimeter wind speed algorithm at high wind speeds. *J. Geophys. Res.*, **98**, 20 275–20 285, doi:10.1029/93JC02117.

——, 1994: Global ocean wave statistics obtained from satellite observations. *Appl. Ocean Res.*, **16**, 235–248, doi:10.1016/0141-1187(94)90023-X.

——, 1998a: An experimental investigation of the role of atmospheric stability in wind wave growth. *Coastal Eng.*, **34**, 23–33, doi:10.1016/S0378-3839(98)00011-8.

——, 1998b: An intercomparison of GEOSAT, TOPEX and ERS1 measurements of wind speed and wave height. *Ocean Eng.*, **26**, 67–81, doi:10.1016/S0029-8018(97)10016-6.

——, 1999: Seasonal variability of the global ocean wind and wave climate. *Int. J. Climatol.*, **19**, 931–950, doi:10.1002/(SICI)1097-0088(199907)19:9<931::AID-JOC412>3.0.CO;2-O.

——, S. Zieger, and A. V. Babanin, 2011: Global trends in wind speed and wave height. *Science*, **332**, 451–455, doi:10.1126/science.1197219.

——, J. Vinoth, S. Zieger, and A. V. Babanin, 2012: Investigation of trends in extreme value wave height and wind speed. *J. Geophys. Res.*, **117**, C00J06, doi:10.1029/2011JC007753.

Zeng, L., and R. A. Brown, 1998: Scatterometer observations at high wind speeds. *J. Appl. Meteor.*, **37**, 1412–1420, doi:10.1175/1520-0450(1998)037<1412:SOAHWS>2.0.CO;2.

Zieger, S., J. Vinoth, and I. R. Young, 2009: Joint calibration of multiplatform altimeter measurements of wind speed and wave height over the past 20 years. *J. Atmos. Oceanic Technol.*, **26**, 2549–2564, doi:10.1175/2009JTECHA1303.1.

——, A. V. Babanin, and I. R. Young, 2014: Changes in ocean surface winds with a focus on trends of regional and monthly mean values. *Deep-Sea Res. I*, **86**, 56–67, doi:10.1016/j.dsr.2014.01.004.